# UPWARD GAS-LIQUID FLOW IN CONCENTRIC AND ECCENTRIC ANNULAR SPACES

A Thesis

by

PEDRO CAVALCANTI DE SOUSA

Submitted to the Office of Graduate and Professional Studies of
Texas A&M University
in partial fulfillment of the requirements for the degree of

MASTER OF SCIENCE

| | |
|---|---|
| Chair of Committee, | Maria Barrufet |
| Co-chair of Committee, | Gioia Falcone |
| Committee Member, | Gerald Morrison |
| Head of Department, | Daniel Hill |

December 2013

Major Subject: Petroleum Engineering

# ABSTRACT

A limited amount of work exists on upward gas-liquid flow in annular spaces. This is a common scenario in drilling operations, especially in underbalanced drilling, and in high-production wells. To carry out this study, a 40-meter high laboratory facility with an annulus flow loop composed of a 5-1/2 in. outer-pipe and a 2-3/8 in. inner-pipe was used, with tap water as the liquid phase and compressed-air as the gas phase.

This work's objective was to phenomenologically characterize gas-liquid flow in annular space, investigate possible causes of unexpected periodic formation of liquid slugs in the annulus, assess potential effects of eccentricity of the inner pipe, extract empirical relationships between two-phase flow parameters (e.g. pressure drop, holdup, and Reynolds, Weber and Froude numbers) for both concentric and eccentric configurations, investigate production hysteresis effects on test results, and test ramp-up sequences to try to mimic possible subsequent accumulation of liquid in the annulus.

The findings from this work revealed that total pressure drops in concentric and eccentric cases are similar at high gas superficial velocities; however, trends suggest that an eccentric inner pipe causes higher pressure drops at low gas superficial velocities. This is probably due to observed local liquid accumulations around the couplings of the inner pipe when in eccentric configuration. The presence of couplings affects the stability of the Taylor bubble in seemingly slug flows. No liquid accumulation was seen in any of the hysteresis or ramp-up scenarios tested. In ramp-up tests, pressure gradient

spikes at the beginning of each test were found to be strongly dependent on the ramp slope.

This work contributes to the understanding of gas-liquid flow phenomena observed in the field, both in wells and in risers, when localized liquid flow reversal and/or accumulation may lead to gas production impairments. This work also sheds some light on how to best operate wells and facilities, and particularly on how to manage production ramp-ups.

# DEDICATION

I dedicate this work to my parents.

# ACKNOWLEDGEMENTS

I would like to thank my committee chair, Dr. Barrufet, my committee co-chair, Dr. Falcone, and my committee member, Dr. Morrison, for their support throughout the course of this research. I would also like to thank Dr. Paulo Waltrich, from the Petroleum Engineering department from Louisiana State University for his help and friendship, and Dr. Carlos Avila from Chevron for his support.

Thanks also go to my officemates, colleagues and friends Akkharachai "Bo" Limpasurat, Andrew Birt, Ardhi Gaol, Arturo Martinez, Bruna Alves, Clarisse and Lauro Porto, Francisco Tovar, Juan Lacayo, Jessica Klement and Ryan Davis, Johannes Alvarez, Katerina Poole, Laura and Márcio Giacomoni, Luan Soares, Marco Molina, Maria Alves, Sergio Gonzales, and Thanita Kiatrabile for making my time at Texas A&M University a great experience.

I would also like to thank the department faculty and staff, especially John Maldonado and student worker Seth Williford for all their help and support in my research.

Finally, thanks to my parents for their encouragement and support.

TABLE OF CONTENTS

Page

LIST OF FIGURES

Page

LIST OF TABLES

Page

# CHAPTER I

# INTRODUCTION AND OBJECTIVES

## Introduction

In deep-water, subsea environment it has become common practice to have separators located at the seafloor as part of the subsea processing. New technologies have emerged to attend the demand for more compact separators, reducing expenditures in the exploration of deep-water plays. These technologies, while more economic, have reduced separation performance and ability to handle changes in flow rates and composition (Hannisdal et al., 2012). With reduced separation performance, the expected one-phase flows through the different production lines give way to multiphase flows, reducing the productivity of gas and liquid at the surface. In the gas-line, the presence of liquid will potentially result in liquid-slugs at the surface (Deuel et al., 2011), which will lead to higher pressure drops in the production line and a decrease in production.

After separation, fluids can be brought to the surface in open pipe risers (Hoffman et al., 2010) or in a pipe-in-pipe configuration (Szucs and Lim, 2005). In the pipe-in-pipe case, liquid is brought to surface through the inner tubular, whereas gas will be carried in the annular space between the external and internal pipes. Since the study of vertical two-phase flow in open pipe has been exhaustively explored in the literature, this work will focus on the vertical two-phase flow in annular spaces.

The real life field situation described above was reproduced in laboratory scale at the TowerLab facility, located inside the Joe C. Richardson Building on the Texas A&M University main campus. This lab has become a reference for this kind of experiment. It extends from the basement of the building up to its 10th floor. The main control of the facility is found at the 6th floor, room 601. TowerLab is composed of two flowloops with different test sections. The first loop consists of 2-in. transparent PVC pipes, whereas the second loop is composed of 2-3/8-in drill-pipe inside an acrylic (and steel) 5-1/2-in. casing, resulting in an annular test section.

TowerLab's annulus flowloop is therefore analogous to the annular space described in the afore-mentioned subsea environments and, for this reason, it was chosen as an instrument to explore the problems discussed above. The annulus configuration from TowerLab is presented in Figure 1.

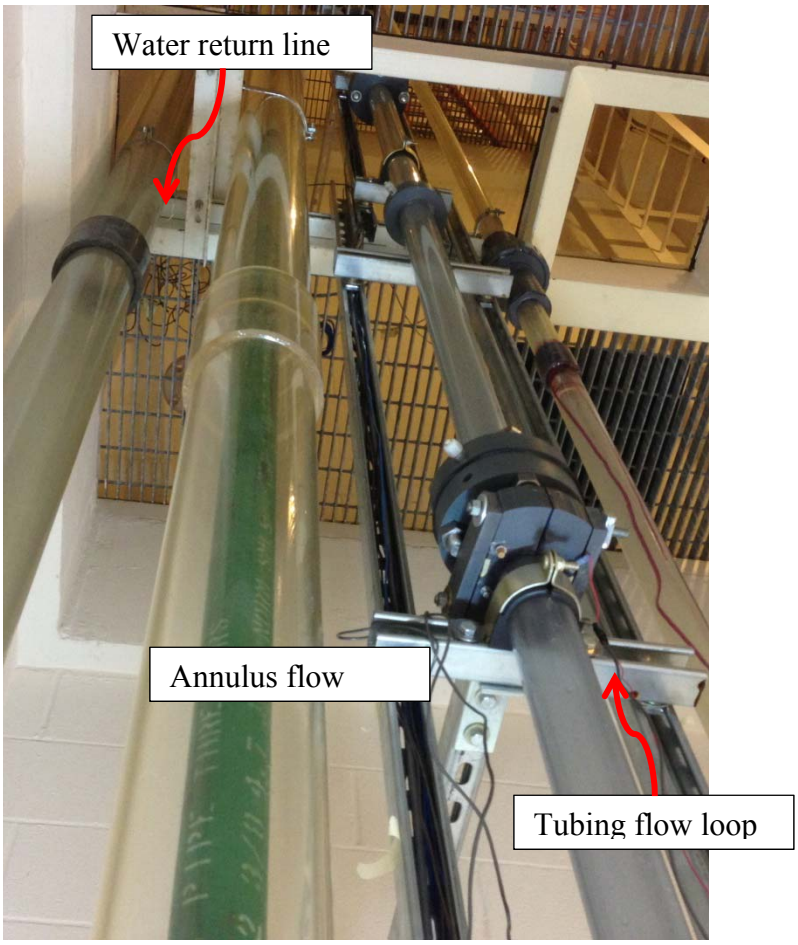


**Figure 1:** TowerLab flow loops.

## Objectives

The objectives of this project were set as follows:

- Investigate possible causes of unexpected periodic release of liquid slugs at the top of annular space lines seen in field applications.
- Mimic the two-phase flow up the annulus in subsea plays by using the concentric flowloop in the TowerLab experimental facility at Texas A&M University.

- Assess the potential effects of eccentricity in the annular space.
- Try to infer empirical relationships between key two-phase flow parameters (e.g. pressure drop, holdup, Reynolds, Weber and Froude numbers) for both concentric and eccentric geometry configurations.
- Assess hysteresis effects on test results.
- Test ramp-up sequences to try to reproduce possible subsequent accumulation of liquid in the annulus along its length.
- Suggest possible directions for future work to upscale the findings from the small-scale experiments in TowerLab to the field scale.

With regards to the first point above, previous investigations by Kiatrabile (2012) excluded the possibility of liquid accumulation as a consequence of pressure/volume/temperature (PVT) fluid characteristics (such as condensate dropout of vapor condensation).

The first step in this study consisted of mapping the operational limits of the facility by a series of steady-state tests. This was necessary to account for modifications and upgrades to TowerLab in the last year. Following this step, another set of tests was run to characterize the transient behavior of two-phase flow in an annulus space.

With these tests, we expected to build a solid database that could not only explain some of the features seen in the field, but also serve as research material to further explore the two-phase flow in annulus spaces.

# CHAPTER II

# LITERATURE REVIEW

To understand the nature of the two-phase flows investigated for this study, it is necessary to appreciate the differences between full-pipe and annulus (concentric or eccentric) upward flows. Below is a summarized review of gas/liquid flow characteristics in both configurations, which highlights the paucity of data and relationships specific to annular flow.

## Gas-liquid flow in pipes

A significant amount of work has been carried out over the years on the characterization of gas/liquid flow inside open (no obstruction) pipes (Waltrich et al., 2013). On the other hand, the flow of two phases inside annulus spaces is very limited and not well understood (Das et al., 2002; Lage and Time, 2000). The degree of eccentricity and the presence of couplings add extra uncertainties to any analysis and, thus, are the greatest challenges faced by this work. The first step to understanding the behavior of gas/liquid flows is by describing how this flow takes place.

Two-phase flow in pipes is characterized by how the gas and liquid phases are distributed during flow. In the case of vertical flow in open pipes, the different patterns are described in the list below (Shoham, 2006) and illustrated in Figure 2 (Taitel et al., 1980).

1. Bubble flow: Characterized by low liquid rates, with the gas phase dispersed in the liquid phase and on a zigzag, upward motion relatively to the liquid.

Slippage (relative movement between two phases) occurs between the gas and the liquid and values of liquid holdup are high (which is further explained in the Liquid holdup section)

2. Dispersed bubble flow: Similar to bubble flow, but with high rates of liquid. Contrary to bubble flow, there is no slippage between the gas and liquid phases in this flow pattern.
3. Slug flow: Large bubbles of gas followed by slugs of liquids. The gas pockets have a bullet shape and are called Taylor bubbles. These bubbles take almost all the space available for flow, but a thin film of liquid is formed around it. The liquid in this film flows downward into the subsequent slug.
4. Churn: Similar to slug flow, but occurring at higher gas rates. The slugs are shorter and frothy and are constantly broken by the air flowing. After the slug is broken, the liquid fall into the following churn, giving the entire flow an oscillatory motion.
5. Annular flow: High gas rate flows in the center of the pipe, carrying over entrained liquid. The liquid phase is found around the pipe wall on an upward motion.

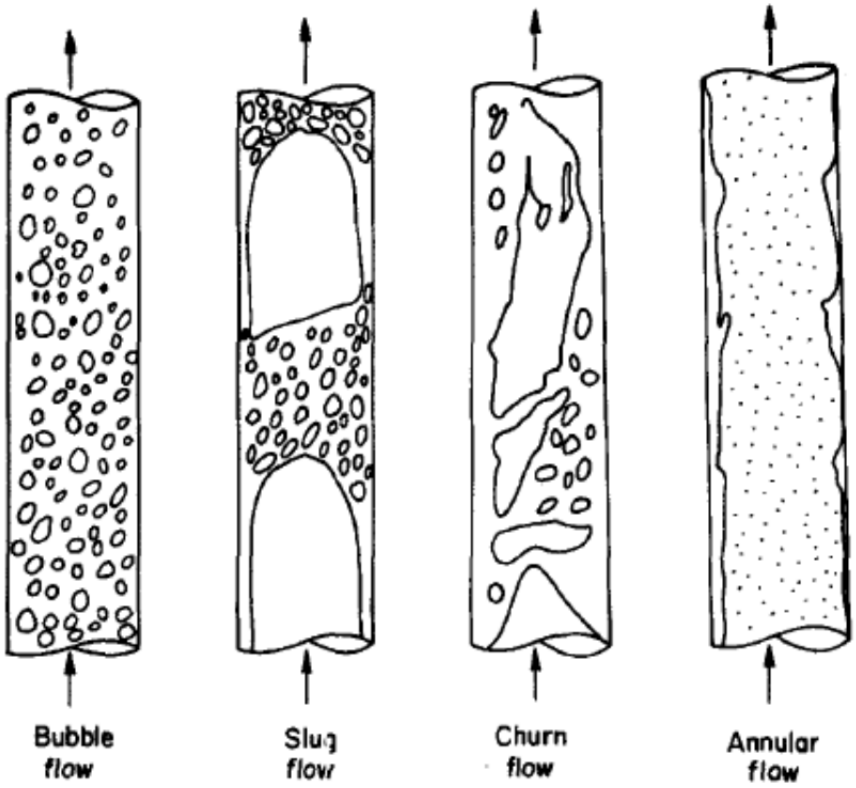


**Figure 2:** Flow patterns in vertical flow (Taitel et al., 1980). Dispersed bubble flow (not shown here) and bubble flow look similar, with the exception that the bubble in dispersed bubble, the bubbles are smaller.

In relation to the present case study, the two-phase flow patterns for concentric and fully eccentric annulus configurations are shown in Figure 3 taken from Caetano et al. (1992). According to this study, the flow regimes in the annulus can be described as follows:

1. Bubble flow: The gas bubbles dispersed inside the liquid phase may take either a spherical or a cap shape. The spherical bubbles will go move upwards in a zigzag motion whereas the cap-shaped bubbles will go straight

up. In fully eccentric configuration, the cap bubbles migrate to the largest gap of the annulus.

2. Dispersed bubble flow: Similar to what is seen in the open pipe case, here too there is no slippage between gas and liquid phases. The gas bubbles are smaller and they all have spherical shape moving upwards with no zigzag motion. Dispersed flow behaves similarly in both concentric and eccentric configurations.
3. Slug flow: Differently to what is seen in open pipe flows, in an annulus geometry the downwards movement of liquid around the Taylor bubble has a preferential channel, making the bubble not symmetric as seen in open pipe flow. In fully eccentric configuration, the preferential channel is always located where the pipes are in contact.
4. Churn flow: Similar to what happens in open pipe flows. This flow pattern does not depend on eccentricity.
5. Annular flow: This flow pattern differs from what it was described previously in that the liquid film is now located not only on the outer wall, but also on the inner tubing wall. The outer film thickness is always greater than that of the inner film. In fully eccentric configuration, liquid will accumulate at the region where the pipes are in contact.

As stated before, few studies have examined two-phase flow in annular space. Even fewer works have tried to establish mechanistic models to predict flow pattern transitions: Caetano et al. (1992) and Lage and Time (2000) modified the model from

Taitel et al. (1980) for open pipes to predict flow patterns in an annular space. Das et al. (2002) modified the previous models to account for asymmetric flow regimes seen in annular spaces.

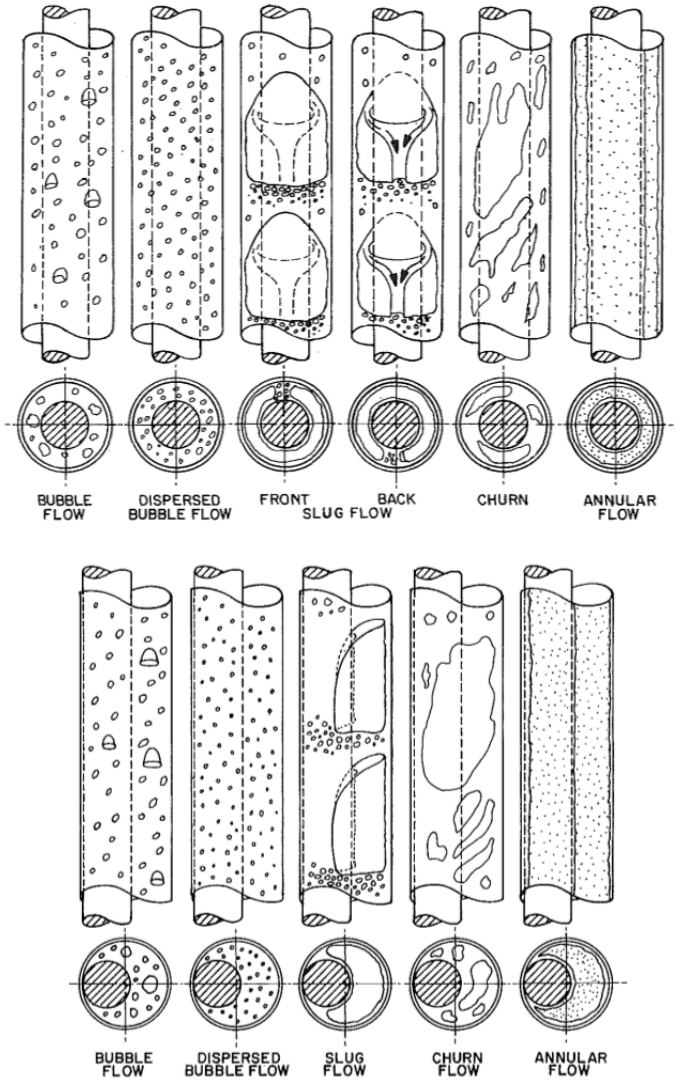


**Figure 3:** Flow patterns in vertical flow for concentric (top) and eccentric (bottom) annulus (Caetano et al., 1992).

Key parameters necessary to define and characterize two-phase flows in both field and laboratory settings are briefly presented below, before the description of the laboratory methodology adopted for this study.

*Liquid holdup*

Liquid holdup – here referred to simply as holdup and symbolized by α – is the fraction of the volume of a gas-liquid flow occupied by the liquid phase. Obviously, the average holdup cannot be equal to zero nor one, since, in those cases, we would end up having either single phase gas or single phase liquid flow, respectively. The local holdup, though, will vary throughout the length of the pipe and it may take values between zero and one.

*Pressure gradient*

The pressure drop over a length L can be calculated by solving the mechanical energy balance equation (Economides et al., 2012):

$$dp + \rho \cdot u \cdot du + \rho \cdot g \cdot dz + \frac{f \cdot u^2}{2 \cdot D} \cdot dL = 0 \tag{1}$$

where $\rho$ is the density of the fluid, $u$ is the velocity of the fluid, $g$ is the acceleration due to gravity, $f$ is the friction factor, and $dL$ is the infinitesimal change in length of the pipe. The dimension $D$ is the characteristic length of the flow which, in pipes, corresponds to the hydraulic diameter ($D_{\mathrm{hyd}}$).

The hydraulic diameter is defined as (Caetano et al., 1992):

$$D_{\mathrm{hyd}} = \frac{4 \cdot A}{P_{\mathrm{wet}}} \tag{2}$$

where $A$ is the cross-sectional area, and $P_{\text{wet}}$ is the wetted perimeter. For the annulus space limited by circles of diameters $D_{\text{in}}$ and $D_{\text{out}}$, where $D_{\text{out}} > D_{\text{in}}$, we have $A = \pi(D_{\text{out}}^2 - D_{\text{in}}^2)/4$, $P_{\text{wet}} = \pi(D_{\text{out}} + D_{\text{in}})$. Thus, the hydraulic diameter is:

$$D_{\text{hyd, annulus}} = D_{\text{out}} - D_{\text{in}} \tag{3}$$

When analyzing perfectly vertical flows we have $dL = dz$. We then divide everything by $dz$, and we rewrite Eq. 1 as:

$$-\frac{dp}{dz} = \rho \cdot u \cdot \frac{du}{dz} + \rho \cdot g + \frac{f \cdot u^2}{2 \cdot D} \tag{4}$$

where $dp/dz$ is the pressure gradient, that is, the pressure drop per increment of length (or height). The three terms on the right-hand side of Eq. 4 are the kinetic, the potential, and the frictional energy components of the pressure drop, respectively. In steady-state flow, the kinetic component is negligible, but in transient analysis, it must be taken into consideration.

*Superficial velocities*

Another important concept in two-phase flow is the idea of superficial velocities, defined as the volumetric flux of a phase, or the volumetric flow per unit area (Shoham, 2006). Thus, for gas and liquid, the superficial velocities ($u_{sg}$ and $u_{sl}$, respectively) are:

$$u_{sg} = \frac{q_g}{A_{\text{annulus}}} = \frac{\dot{m}_g}{\rho_g \cdot A_{\text{annulus}}} \tag{5}$$

$$u_{sl} = \frac{q_l}{A_{\text{annulus}}} = \frac{\dot{m}_l}{\rho_l \cdot A_{\text{annulus}}} \tag{6}$$

where the variable $q$ represents the volumetric rates and $\rho$, the density and the indeces $l$ and $g$ stand for liquid and gas, respectively. $A_{\text{annulus}}$ is the area of the annulus.

*Dimensionless two-phase parameters*

The use of scaled models generally preserves geometric similarity between laboratory experiments and real-life phenomena. However, for an accurate representation of any given system, model studies must respect a dynamic similarity. Following this approach, we are required to reproduce in a laboratory environment the same values of relevant dimensionless parameters as those seen in actual systems (Tavoularis, 2005).

In case of two-phase flow, numerous empirical correlations have been developed as means to obtain pressure drop calculations in real-world applications. The use and limitations of these methods are out of the scope of this work; however, a few of them were used as a basis to define important dimensionless numbers used in flow analysis. Thus, Reynolds, Weber and Froude numbers were chosen as two-phase flow parameters to be used in dimensionless analysis and their mathematical definitions were taken from benchmark publications in the oil and gas industry.

The Reynolds number was originally conceived to describe single-phase, incompressible flows; however, it has also been used in two-phase flows such as indicated in Hagedorn and Brown (1965):

$$Re = \frac{D_{\mathrm{hyd}} \cdot u_m \cdot \bar{\rho}}{\mu_l^{\alpha} \cdot \mu_g^{(1-\alpha)}} \tag{7}$$

where $D_{\mathrm{hyd}}$ is the hydraulic diameter as defined previously, $\mu_l$ and $\mu_g$ are the viscosity of the liquid and gas phases, and $\alpha$ is the liquid holdup. The other parameters are defined below. First the velocity of the mix $u_m$:

$$u_m = u_{sg} + u_{sl} \tag{8}$$

and the average density $\bar{\rho}$:

$$\bar{\rho} = \alpha \cdot \rho_l + (1 - \alpha) \cdot \rho_g \tag{9}$$

The Weber number represents the ratio of the inertia to the surface tension forces and is defined as (Tavoularis, 2005):

$$We = \frac{\rho_{\mathrm{l}} \cdot V^2 \cdot D_{\mathrm{hyd}}}{\sigma_{g/l}} \tag{10}$$

where $\sigma_{g/l}$ is the surface tension between the gas and the liquid, and $V$ is the characteristic velocity of the flow. In our case, we considered $V = u_{sg}$.

Finally, the Froude number represents the ratio of inertia to gravitational forces, being applied mainly to liquid flow with free surface (Tavoularis, 2005). It is defined in Beggs and Brill (1973) as:

$$Fr = \frac{u_m^2}{g \cdot D} \tag{11}$$

**Properties of fluids**

Air and water properties were computed by methods indicated in the literature, with the exception of the density of water, which was obtained in laboratory with a procedure described in Chapter III.

*Density of air*

The density of air is calculated according to the simplified formula recommended by the National Institute of Standards and Technology (NIST). The general form of the equation is given in Picard et al. (2008):

$$\rho_{\text{air}} = \frac{p \cdot (1 - 0.3780 \cdot x_v) \cdot 10^{-3}}{Z \cdot T} \left[3.483740 + 1.4446 \cdot \left(X_{\text{CO}_2} - 0.0004\right)\right] \quad (12)$$

where $Z$ is the air compressibility factor, $T$ is the temperature in Kelvin, $X_{\text{CO}_2}$ is the molar fraction of carbon dioxide in the air composition and $x_v$ is given by:

$$x_v = h \cdot f(p,T) \cdot \frac{p_{sv}(T)}{p} \quad (13)$$

where $h$ is the relative humidity of air, $f(p,T)$ is called the enhancement factor, and $p_{sv}(T)$ is the vapor pressure for air at a given temperature.

Eq. 12 is simplified with the following assumptions:

1. $Z$ = 1, due to the low pressures
2. $X_{CO_2}$= 0.0004, which is the standard value according to Picard et al. (2008)
3. $h$ = 0, since the air from the compressor is delivered to the system dry.

With these assumptions, the air density is given by:

$$\rho_{\text{air}} = 3.483740 \cdot 10^{-3} \frac{p}{T} \quad (14)$$

*Viscosity of air*

The viscosity of air is calculated with Eq. 15 (Lemmon and Jacobsen, 2004).

$$\mu = \mu^0(T) + \mu^r(\tau, \delta) \quad (15)$$

where $\mu$, $\mu^0$ , and $\mu^r$ are the total, the dilute gas and the residual viscosities, all given in μPa.s.

$$\mu^0(T) = \frac{0.0266958 \cdot \sqrt{\mathrm{MW} \cdot T}}{\sigma^2 \cdot \Omega(T^*)} \tag{16}$$

where MW is the molecular weight of air in g/mol, $T$ is the temperature in Kelvin, $\sigma$ is the Lennard-Jones size parameter (0.360 nm for air), and Ω is the collision integral given by:

$$\Omega(T^*) = \exp\left\{\sum_{i=1}^{5} b_i \cdot [ln(T^*)]^{i-1}\right\} \tag{17}$$

with

$$T^* = \frac{T}{\varepsilon/_k} \tag{18}$$

where $\varepsilon/k$ is the Lennard-Jones parameter. For air, this parameter is equal to 103.3 K.

The residual viscosity is given by:

$$\mu^r(\tau, \delta) = \sum_{i=1}^{5} N_i \cdot \tau^{t_i} \cdot \delta^{d_i} \cdot \exp(-\gamma_i \cdot \delta^{l_i}) \tag{19}$$

with $\gamma_i = 0$ for $l_i = 0$ and $\gamma_i = 1$ for $l_i \neq 0$ and all other parameters are given in Table 1 below.

**Table 1:** Dimensionless parameters for $\mu^0$ and $\mu^r$ equation.

| $i$ | $b_i$ | $N_i$ | $t_i$ | $d_i$ | $l_i$ |
|---|---|---|---|---|---|
| 1 | 0.431 | 10.72 | 0.2 | 1 | 0 |
| 2 | -0.4623 | 1.122 | 0.05 | 4 | 0 |
| 3 | 0.08406 | 0.002019 | 2.4 | 9 | 0 |
| 4 | 0.005341 | -8.876 | 0.6 | 1 | 1 |
| 5 | -0.00331 | -0.02916 | 3.6 | 8 | 1 |

*Density and viscosity of water*

The dependency of water density on temperature and pressure was not considered in this study. Temperature variations between tests are within 20 and 30°C (68 and 86°F), which, at atmospheric pressure, results in a 0.26% change in density (Haynes, 2012). This change in value is well within the average measurement error (2.12%) and, thus, can be neglected. The same can be said in respect to pressure. Figure 4 below reflects the small dependency of the density of water with pressure (given in MPa) and temperature (Schmelzer et al., 2005). In TowerLab, the pressure range varies from 0.1 to 1.0 MPa.

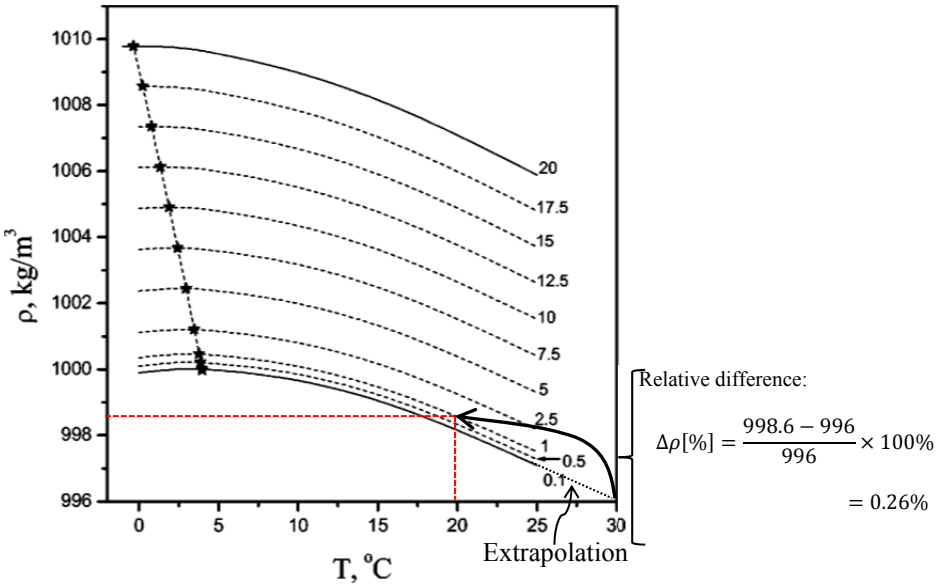


**Figure 4:** Dependency of density of water with pressure and temperature (Schmelzer et al., 2005). The relative difference calculation is shown on the side and it is graphically indicated by the bold black arrow.

With density being constant, viscosity of water is dependent only on temperature (IAPWS, 2003). In this report, the viscosity of water is given by Eq. 20:

$$\mu = \bar{\mu} \cdot \mu^* \tag{20}$$

where $\mu^*$= 55.071 μPa.s and

$$\bar{\mu} = \bar{\mu}_0(\bar{T}) \cdot \bar{\mu}_1(\bar{T}, \bar{\rho}) \cdot \bar{\mu}_2(\bar{T}, \bar{\rho}) \tag{21}$$

with $\bar{T} = T/T^*$, $\bar{\rho} = \rho/\rho^*$, $T^*$ = 647.226 K and $\rho^*$ = 317.763 kg/m$^3$, and $\bar{\mu}_0$, $\bar{\mu}_1$ and $\bar{\mu}_2$ being called partial viscosities.

The partial viscosities are given by:

$$\bar{\mu}_0(\bar{T}) = \frac{\sqrt{\bar{T}}}{\sum_{i=0}^{3} \frac{H_i}{\bar{T}^i}} \tag{22}$$

$$\bar{\mu}_1(\bar{T},\bar{\rho}) = \exp\left[\bar{\rho}\cdot\sum_{i=0}^{5}\sum_{j=0}^{6} H_{ij}\cdot\left(\frac{1}{\bar{T}}-1\right)^{i}\cdot(\bar{\rho}-1)^{j}\right] \tag{23}$$

and $\bar{\mu}_2(\bar{T},\bar{\rho}) = 1$ for pressures and temperatures not near the critical point. The $H_i$ and $H_{ij}$ coefficients are given in Tables 2 and 3, respectively.

**Table 2:** Coefficients $H_i$ for calculation of partial viscosity $\bar{\mu}_0$.

| $i$ | $H_i$ |
|---|---|
| 0 | 1 |
| 1 | 0.978197 |
| 2 | 0.579829 |
| 3 | -0.20235 |

**Table 3:** Coefficients $H_{ij}$ for calculation of partial viscosity $\bar{\mu}_1$.

| $i$ \ $j$ | 0 | 1 | 2 | 3 | 4 | 5 | 6 |
|---|---|---|---|---|---|---|---|
| 0 | 0.513205 | 0.215178 | -0.28181 | 0.177806 | -0.04177 | 0 | 0 |
| 1 | 0.320566 | 0.731788 | -1.07079 | 0.460504 | 0 | -0.01578 | 0 |
| 2 | 0 | 1.241044 | -1.26318 | 0.234038 | 0 | 0 | 0 |
| 3 | 0 | 1.476783 | 0 | -0.49242 | 0.160044 | 0 | -0.00363 |
| 4 | -0.77826 | 0 | 0 | 0 | 0 | 0 | 0 |
| 5 | 0.188545 | 0 | 0 | 0 | 0 | 0 | 0 |

From that the Equations and Tables above, we can conclude that, for a fixed density ($\rho_{\mathrm{water}}$), viscosity only depends on temperature. The dependency on temperature can be obtained by plotting viscosities versus temperatures. From that we fitted a polynomial of order four to obtain Eq. 24:

$$\begin{aligned}\mu(T) = {} & 1.1542\times10^{-7}\cdot T^4 - 1.9018\times10^{-5}\cdot T^4 + \\ & + 1.3633\times10^{-3}\cdot T^2 - 5.9843\times10^{-2}\cdot T + 1.7868\end{aligned} \tag{24}$$

## Modeling of gas-liquid flow

As stated before, upward, two-phase flow in annulus space has several applications. Notably, in the oil industry this scenario is present in high-productivity wells and also in drilling operations (Lage and Time, 2000). The analysis of steady-state multiphase flow in pipes has two distinct approaches: the first one relies on empiricism and a second one is based on mechanistic description of the flow (Ellul et al., 2004). In this work we will focus on the mechanistic approach, where the pressure drop is determined as a function of the different flow patterns described previously (Lage and Time, 2000).

The simplest analysis we can perform is based uniquely on Eq. 1 between two points (say, A and B). In steady-state the velocity is constant, thus the velocity term vanishes. Furthermore, the absolute pressure is measured directly on TowerLab and the potential energy term is only dependent on the height of the column of fluid, which is also known. The only term we are left to calculate is the one related to friction losses. In this term we know the length between points (which, for perfectly vertical case, corresponds to the height difference) and the characteristic velocity, which we took as the superficial gas velocity. Thus, we are left with the following equation:

$$(p_A - p_B) + \rho \cdot g \cdot (z_A - z_B) + \frac{f \cdot u_{sg}^2}{2 \cdot D_{\text{hyd}}} \cdot (z_A - z_B) = 0 \qquad (25)$$

where $f$ is unknown.

The friction factor for one-phase flow is obtained from the Moody chart or from iterative processes. However, an approximation for $f$ is given in Economides et al. (2012) as:

$$\frac{1}{\sqrt{f}} = -2.0 \cdot log\left(\frac{k}{3.7065} - \frac{5.0452 \cdot log\left(\frac{(k)^{1.1098}}{2.8257} + \frac{5.8506}{Re^{0.8981}}\right)}{Re}\right) \quad (26)$$

where $k$ is the relative roughness of the pipe. In our case, we used $k = 0.006$.

This equation results in accurate values with the advantage that no graphical analysis or iterative methods are required. Since there is no simple way to determine to two-phase flow friction factor, we have chosen to use Eq. 26, despite the fact that it will, most probably, underestimate the friction factor significantly.

*Numerical simulation with OLGA 7*

OLGA is a commercial program available on the market since 1990. Its applications range most aspects of the production system in the oil industry, covering from bottom hole to process equipment. OLGA is a three-fluid model (gas, water and oil) which recognizes two basic flow regime classes: distributed and separated. The distributed flow can either be bubble or slug flow, whereas the separated flow is stratified (which does not apply to vertical flow) or annular. For further information on OLGA, we recommend the software User Manual, version 7.2.1.

**Measurements in fluid mechanics**

The properties and parameters inferred from laboratory or field tests depend directly on the quality of the data acquired. This section describes in general lines how

the equipment used to measure the fluid and flow properties work and how accurate the measurements are.

*Flow measurements*

Measuring flow rates is one of the most important aspects of any research in fluid mechanics. These measurements are not concerned with local velocity variations across the cross section, but they are conceived to measure the amount of fluid passing through a certain cross section per unit of time. The measurement can be either in terms of volume or mass (Tavoularis, 2005). Several types of instrument for measuring flow are available on the market, but explaining how each equipment work is outside the scope of this work. In the following paragraphs, the principle behind the models of flow meters used in our tests are briefly explained

**Vortex flowmeter**

The main part of this piece of equipment is a bluff object immersed in the flowing fluid that spans the cross section of the pie. The presence of this object produces vortices at a certain frequency, which, in turn, can be correlated with the velocity of the fluid flowing (Goldstein, 1996; Tavoularis, 2005). Once the velocity has been determined, the volumetric flow rate is inferred from the diameter of the pipe.

**Coriolis flowmeter**

This kind of flow meter is very versatile in that it is able to measure mass flow rates independently of fluid properties or flow conditions. It relies on the fact that the flowing fluid will pass through a bent tube, applying force to it. Since the tube cannot bend, it is set to vibrate by a magnetic field generated inside the equipment. The

magnitude of force applied to the tube will then make it twist at a given angle which can be readily correlated to the mass flow rate (Goldstein, 1996; Tavoularis, 2005).

### *Pressure measurement*

There exist several methods of measuring pressure. It is also outside the scope of this work to describe how the different equipment work, so we focus on the one used on our tests. The pressure measuring instrument by choice was electrical pressure transducer. This device sends an electric signal that responds either linearly or non-linearly to the absolute or gauge pressure. Calibration of the instrumentation must be made on installation and periodically thereafter. The greatest advantage of electric pressure transducers is their frequency response, being capable of delivering several readings in a short time. The disadvantage of using this kind of transducer is that the pressure readings must be done at the walls of the test section. That arrangement does not allow for actual readings of absolute or gauge pressure but rather indicates the pressure fluctuations inside the boundary layer (Goldstein, 1996; Tavoularis, 2005).

### *Assessing measurement uncertainty*

Measuring systems will generate one or more output as a response to some input, or set of inputs. When all the inputs and outputs are constant or varying very slow with time, the operation is said to be static. If at least one of the inputs is time dependent the operation is called dynamic (Tavoularis, 2005).

In this research, both steady-state and transient flows were performed, but, since only steady-state flow regimes were used to characterize the facility, we will focus on the static response of the measuring system, that is, the response to the static operation

mode. The dynamic response of measuring systems is only important in transient flows, but even in those cases it is only relevant if the response time of the measuring system itself is in the same order of magnitude (or higher) of the response time from the facility being used for the tests. In the situation described, the damping of the measuring system would be so large that it might not be able to follow the changes happening during the test and then creating a false delay between input and output. In the case of TowerLab, however, the damping associated with the measuring system is at least 100 times smaller than any change in flow regime that may occur in the facility.

**Normality test and removal of outliers**

Measurements are susceptible to either systematic or random errors. Whereas systematic errors can be identified and removed, random ones are not easily removable. One way assess how random effects might be affecting the measurements made is by performing the $\chi^2$ (chi-square) goodness-of-fit test (Tavoularis, 2005). In the present case, it is assumed that the measurements recorded follow a Gaussian distribution from which both the average ($\mu$) and the variance ($\sigma^2$) were computed as indicated by the equation below.

$$\mu = \frac{1}{N}\sum_{i=1}^{N} x_i \tag{27}$$

$$\sigma^2 = \frac{1}{N-1}\sum_{i=1}^{N} (x_i - \mu)^2 \tag{28}$$

where $N$ is the sample size and $x_i$ are each one of the measurements recorded.

Once these parameters have been calculated, we follow the general procedure given by Montgomery and Runger (2007) and adapted here for the specific case of this work. First, we divide the sample into $k$ class intervals, such that the $j^{\text{th}}$ class ($k_j$) has $n_j$ samples and is bounded by the values $k_{j,\,\text{bottom}}$ and $k_{j,\,\text{top}}$, for $j = 1, 2, \ldots, k$. We also set $k_{1,\,\text{bottom}} = -\infty$ and $k_{k,\,\text{top}} = +\infty$, and add the constrain $k_{j,\,\text{top}} = k_{j+1,\,\text{bottom}}$. When defining $k$, Tavoularis (2005) recommends $k = 1.87 \cdot (N-1)^{0.4}$ and $n_j \geq 5$.

According to Montgomery and Runger (2007), the next step consists of computing the expected frequency ($E_j$) for the interval $k_j$, which is given by:

$$E_j = \int_{k_{j,\,\text{bottom}}}^{k_{j,\,\text{top}}} \frac{1}{\sqrt{2\pi}\cdot\sigma} \cdot exp\left(\frac{-(x-\mu)^2}{2\cdot\sigma^2}\right) \cdot dx \tag{29}$$

that is, the probability of a measured value fall between the $k_j$ boundaries in a normal distribution: $E_j = P\left(k_{j,bottom} \leq x \leq k_{j,\text{top}}\right)$. With these values calculated, the $\chi^2$ value for the set of measurements is:

$$\chi_0^2 = \sum_{j=1}^{k} \frac{\left(F_j - E_j\right)^2}{E_j} \tag{30}$$

where $F_j = n_j/N$.

Once $\chi_0^2$ is computed, we need to test the initial normal distribution hypothesis. The hypothesis should be rejected if $\chi_0^2 > \chi_{\alpha,k-\varphi-1}^2$, where $\alpha$ is the confidence level (set as 95%) and $\varphi$ is the number of parameters of the hypothesized distribution estimated by sample statistics, which in our case is $r = 2$ (mean and variance). Thus, the hypothesis of normal distribution **is not** rejected if:

$$\chi_0^2 \leq \chi_{0.95,k-3}^2 \tag{31}$$

In case the hypothesis is rejected after the chi-square test, it is recommended that the initial set of data be revised by eliminating any outlier in it. NATO (1994) define these as points which appear to be spurious and they are identified, among several other methods, by Chauvenet's criterion. A data point ($x_i$) is considered as an outlier if:

$$|x_i - \mu| \geq \tau \cdot \sigma \tag{32}$$

where $i = 1, 2, \ldots, N$, and the parameter $\tau$ is given by:

$$\tau = \sum_{m=1}^{5} A_m \cdot \left(ln(N)\right)^m \tag{33}$$

where the coefficients $A_m$ are given in Table 4.

**Table 4:** Coefficients $A_m$ for calculation of Chauvenet's parameter.

| $m$ | $A_m$ |
|---|---|
| 0 | 0.720185 |
| 1 | 0.674947 |
| 2 | -0.0771831 |
| 3 | 0.00733435 |
| 4 | -0.00040635 |
| 5 | 0.00000916028 |

**Quantifying uncertainty**

Uncertainty is defined as the interval within which the true value of a measured property $x$ lies at a given confidence level. International convention defines a 95% confidence level as standard practice (Tavoularis, 2005), which will be adopted in this work.

As stated before, two types of errors will occur in any measurement: systematic and random errors, from this point on called bias and precision errors, respectively. Bias errors are constant throughout the experiment, whereas precision errors are the result of undesirable inputs that add to each other, having an unpredictable total effect on the final measurement (Tavoularis, 2005).

Let $r$ be any property given as a function of $J$ independent variables, we write:

$$r = r(X_1, X_2, \dots, X_J) \tag{34}$$

The bias and precision errors contribute to the uncertainty ($u$) of the measurement such that (NATO, 1994):

$$u = \sqrt{B^2 + P^2} \tag{35}$$

where $B$ and $P$ are the bias and precision limits of the property $r$, respectively.

This uncertainty calculation assures with 95% confidence that a measured property $r$ will lay in the interval $[\bar{r} - u,\ \bar{r} + u]$, where $\bar{r}$ is the average of the property $r$. The same concept can obviously be applied to single variable measurements $x$.

*Calculating bias limit*

The bias limit ($B$) is the maximum value the true (but unknown) bias error can take (Tavoularis, 2005). It is the result of a variety of factors, like calibration errors, data acquisition errors, data reduction errors, test technique errors etc. (NATO, 1994). The final bias limit of each $X_j$ is computed as:

$$B_j = \sqrt{\sum_{i=1}^{M} (B_j)_i^2} \tag{36}$$

where $i$ represents each one of the $M$ factors affecting the measurements. The bias limit for the property $r$ in Eq. 34 is calculated as follows:

$$B = \sqrt{\sum_{j=1}^{J} \left( \frac{\partial r}{\partial X_j} \cdot B_j \right)^2} \tag{37}$$

Other terms might be present in Eq. 37 for cases where the biases of two or more measuring systems are correlated. However, since all measurements in the present study are independent, these terms were not presented.

*Calculating precision limit*

The precision limit ($P$) establishes the interval within which the average of measurements will lie, assuming a Gaussian distribution. With a 95% confidence interval, the precision limit of the computed property $r$ from Eq. 54 is (NATO, 1994):

$$P_r = \frac{2\sigma_r}{\sqrt{K}} \tag{38}$$

where $\sigma_r$ is the standard deviation of the $K$ recorded measurments made to compute property $r$, that is:

$$\sigma_r = \frac{1}{K-1} \sum_{k=1}^{K} (r_k - \mu_r)^2 \tag{39}$$

where $\mu_r$ is the average of the property $r$, given by:

$$\mu_r = \frac{1}{K} \sum_{k=1}^{K} r_k \tag{40}$$

It is assumed that all $X_j$ variables in Eq. 34 were determined as **averages over appropriate time periods**. When this is the case, the $k^{\text{th}}$ recorded reading – that is, $\left(X_j\right)_k$ – is evaluated as an individual test and thus the equations 38 through 40 are valid.

# CHAPTER III

# METHODOLOGY

In this section we describe the experimental procedure used for all tests run with TowerLab. The experiments that took place in the development of this project can be summarized in the following steps: (1) map the facility to determine its range of operation, (2) narrow tests to conditions relevant to field case, (3) study liquid behavior along the annulus length (especially where couplings between drilling pipes are located) with fixed gas and liquid rate inputs, and (4) mimic ramp-up procedures and run hysteresis tests. The procedures implemented for each of these steps are explained in the following paragraphs.

## Determination of water density

The density of water was determined in the laboratory simply by using a scale with a 0.01 g precision and a glass flask of known volume ($V_F$) equal to 250 ml. After carefully washing the glass container, it was placed in an oven at 80 °C for one hour. It was then removed from the oven and weighted ($W_E$). Once the temperature dropped enough for the container to be handled, it was filled with tap water (the same used in the experiments) up to the volume mark and it was weighted again ($W_F$). The weight of water in the flask was determined as:

$$W_W = W_F - W_E \tag{41}$$

This weight was divided by the known volume of water and the density of water was given by:

$$\rho_W = \frac{W_W}{V_F} \tag{42}$$

The average value for the density of water was 997.3 kg/m$^3$.

**Description of TowerLab annular flowloop**

During this study, only the annular space flowloop was used. In this text, we will refer to the outer pipes as **casing** and the inner pipe as **tubing**. Figure 5 shows a schematic drawing of the TowerLab annular space flowloop with its main components. All the acronyms are listed and explained further in the text. Figure 6 shows the dimensions of the TowerLab annulus.

As can be seen from Figure 5, the air and water are mixed together before entering the facility at a tee junction, called a mixing tee. Upstream of the mixing tee, the two phases are delivered by two independent systems, whereas downstream, the two phases flow together up a vertical annular space. The characteristics of each system are described in the following sections.

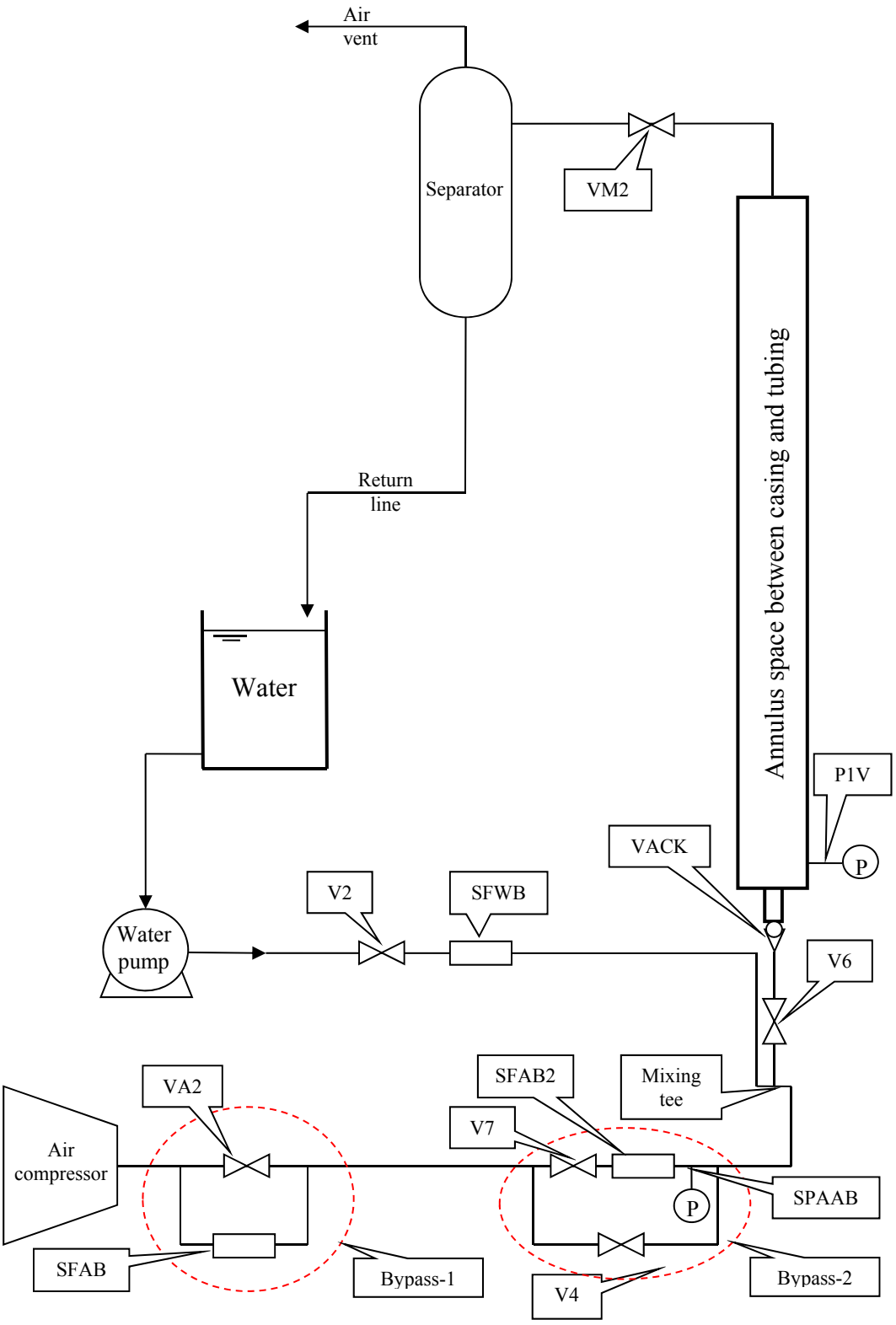


**Figure 5:** Schematics of TowerLab annulus flowloop.

The acronyms in Figure 5 are related to the code used in the data acquisition system and are explained below. The accuracy and measurement ranges of the equipment are also given in the following sections.

- SFAB: Coriolis flowmeter for air (Elite Micro Motion CMF050)
- SFAB2: Vortex flowmeter for air (Rosemount 8800D)
- SFWB: Coriolis flowmeter for water (Micro Motion F100)
- SPAAB: Pressure measurement downstream SFAB2
- P1V: Pressure transducer at test section entry point (Validyne DP 15)
- VA2: Valve to open or close Bypass-1
- V2: valve controlling air rate
- V4: valve controlling intermediate flow rates in Bypass-2
- V6: quick action valve downstream mixing tee
- V7: valve controlling high flow of air
- VM2: annulus test section choke valve
- VACK: check valve downstream V6 to avoid return of water

*The air system*

The air is delivered to the system through the use of an air compressor (Ingersoll Rand 75H-SP), located in the basement of the building, with maximum mass rate capacity of 620 kg/h. Downstream of the air compressor, as indicated in Figure 5, the airline has two bypasses. By adjusting valve openings in each bypass, we are able to operate the facility up to three different thresholds: 100 kg/h, 400 kg/h, and 620 kg/h. The highest threshold is obtained by first having the valve VA2 in Bypass 1 open and

valve V4 closed. The air rate that goes to the mixing tee is then controlled by operating valve V7. To reduce the maximum air rate to the 400-kg/h threshold, valve VA2 in Bypass 1 is closed. This redirects the entire air flow to the SFAB flowmeter (accuracy of ±0.05% of measured rate). The dimensions of SFAB (1/2-in, diameter) restrict the flow to a maximum of 400 kg/h. With V4 closed, we can control the air flow through valve V7. To operate below the 100-kg/h threshold, the air flow must be restricted again. This is achieved by fully closing valve V7 in Bypass 2 and controlling the flow rate by the use of V4. When V4 is fully open, the maximum flow rate reached is 100 kg/h.

The importance of the different thresholds is that they allow for a more precise control of the air rates since they limit the range in which the experiments are run. The minimum air rate is always zero; however, when possible, the experiments were run such that the air rates were limited between 0 and 100 kg/h for the first threshold, 100 and 400 kg/h for the second, and 300 and 620 kg/h for the third.

In the cases of the first two thresholds, the air mass rates are measured directly from SFAB (a Coriolis flowmeter). However, when this flowmeter is bypassed (by opening VA2), measurements must be made with the volumetric flowmeter SFAB2 (accuracy of ±1% of the measured rate), found downstream of valve V7. Following SFAB2 there is a Rosemount pressure meter (SPAAB), model 1151, calibrated to read pressures ranging from 0 to 200 psig with a 0.075% accuracy, and a thermocouple wire for measuring the temperature. The mass rate is then calculated using Eq. 43 below:

$$\dot{m}_a = \frac{q_a}{\rho_a} \tag{43}$$

where the volumetric air rate ($q_a$) is the parameter directly measured by SPAAB and the density of air ($\rho_a$) is determined by Eq. 14.

*The water system*

The water is boosted from a water tank into the system by the use of a centrifugal pump (Dayton, model 2PC39). The pump can deliver up to 2000 kg/h and the water mass rate is measured downstream from the pump by another Coriolis flowmeter (SFWB), which has an accuracy of ±0.10% of the measured rate. The water is also filtered before it is mixed with the air in order to prevent any solid impurities from going into the test facility. The water used in the facility is circulated back to the water tank by the use of a separator located on the 10$^{th}$ floor of the building. The air from the separator is expelled to the atmosphere through an air vent. The flow of water is controlled by both the rotation of the pump and the opening of the valve V2.

*The test section*

The test section includes everything from the valve V6 to the choke valve VM2, located on the 10$^{th}$ floor and situated just upstream of the separator. Besides those valves, the main components of the test section are the pipes themselves and the check valve called VACK, all of which are shown in Figure 6.

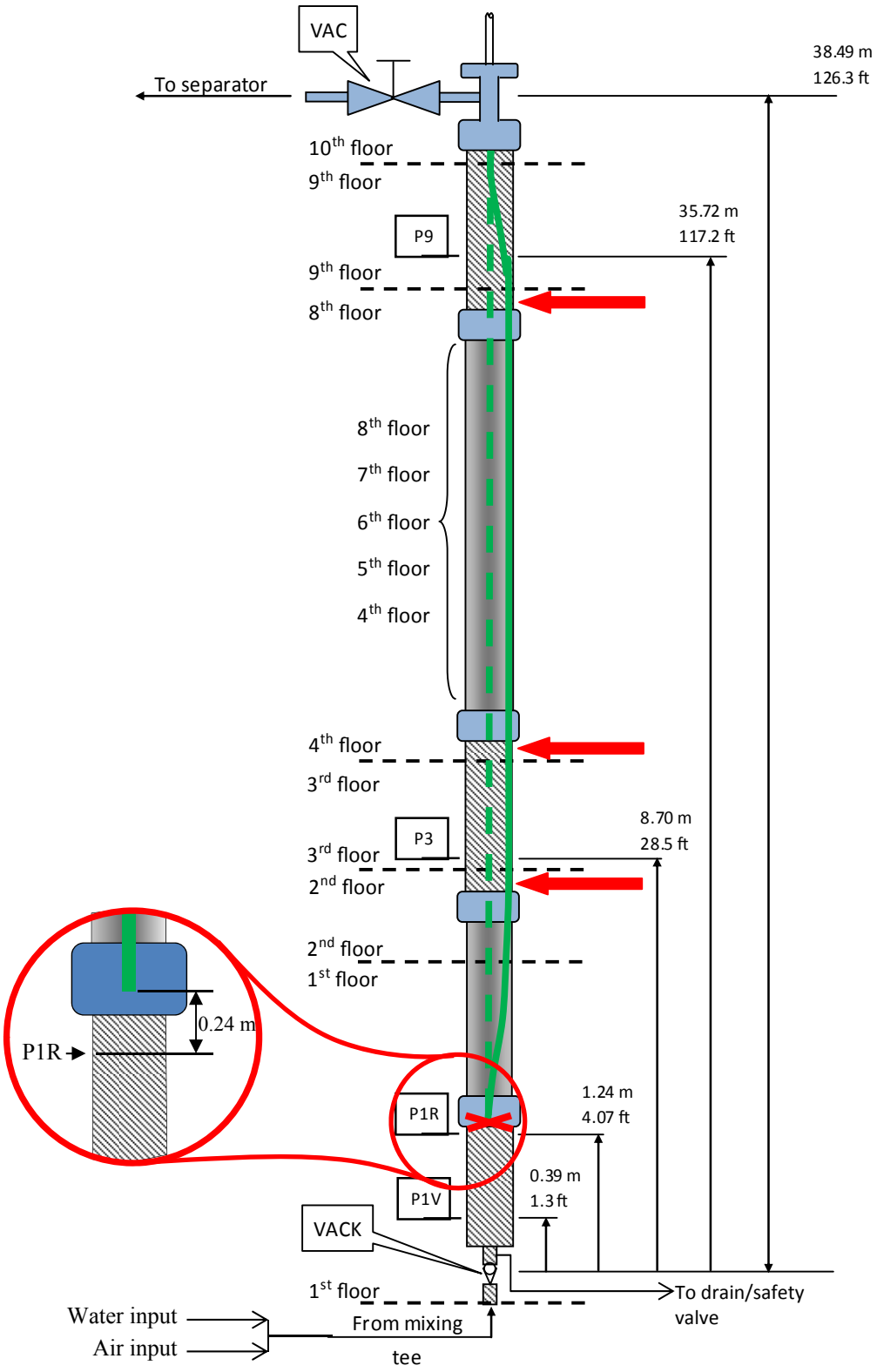


**Figure 6:** Detailed schematic drawing of the annulus flowloop test section.

**Status of facility prior to project and modifications implemented**

Before the start of this project, the annulus flowloop was equipped with only two pressure measurements: one at the mixing tee and another one downstream of the choke valve (VM2), all seen in Figure 6. Some challenges had to be faced to achieve all the objectives proposed for this project. The main challenges were to measure pressure at different points along the facility, automate the annulus flowloop facility, measure holdup, implement constant rate opening of valves in a given time, and guarantee the integrity of TowerLab.

The first problem was solved by installing new pressure transducers to the data acquisition system. We added four more pressure taps along the casing. Their positions are indicated in Figure 6 by the dimension lines.

The operation of the annulus flowloop in TowerLab was very limited. Upstream of the mixing tee there was a manual valve which was connected to the facility itself by a rubber hose. The valve controlling air intake had to be operated manually if air rates higher than 400 kg/h were desired. This air valve was replaced by an automated pneumatic valve (V7), whereas the one upstream of the mixing tee was replaced by a quick action ball valve (V6). The rubber hose was replaced by galvanized pipes, and a check valve (VACK) was installed. The configuration of valves and position of pressure meters before modifications made it impractical (if not impossible) to have holdup measurements such as the ones of today. Another important modification to TowerLab did not come as a physical upgrade, but as a computational routine modification. The simple implementation on LabView that dealt with the valve opening had to be replaced

by a more intricate routine that would let the facility operator chose initial and final opening stages for the valves and the time to go from one to the other. This implementation was required for the ramp-up tests.

Another important feature in today's TowerLab is the safety valve connected to the input of the test section (upstream VACK) as it is indicated in Figure 6. This valve opens if the pressure at the bottom of the test section reaches values higher than 100 psig. This is done to guarantee the integrity of the acrylic pipes. It also allows us to drain the facility in case it is necessary.

Moreover, the facility lacked centralizers. The tubing was held in place at the top ($10^{th}$ floor), where it entered the casing in a centered position, and its lateral movements had no restrictions throughout the entire length of the test facility. Positioners were installed along the facility and they are explained in details in the Section entitled "Eccentricity of the tubing in the annular space".

**The annulus space**

It is important to note that the casing has three sections in steel pipes and two in acrylic, whereas the tubing is formed of the same steel pipe from top to bottom. Figure 6 shows in detail where the sections in acrylic (solid blocks) and in steel (hatched blocks) are located throughout the facility. The blue rectangles seen at the acrylic/steel transitions correspond to dresser joints, used to change from one material to another. The dimension lines seen on Figure 6 indicate the location of the pressure transducers and their height in relation to VACK. The reasons why this check valve was chosen as the reference datum for pressure measurements are explained in the Section "Operations". In

Figure 6 we can also see a zoom that shows in detail the position of the bottom of the tubing in relation to the pressure transducer P1R.

**Operations**

As stated before, TowerLab is operated from a laboratory located in room 601 inside the Richardson Building. In this lab a data acquisition system is connected to a computer, and from there the operator can control almost the entire facility. The operation of the facility goes beyond the scope of this report and it will not be described here; however, it is important to be clear on how the tests are controlled from Lab 601.

The key variables used as test guides are mass rates of air and water. These rates are controlled by the valve openings. The exact opening of a valve to deliver a specified rate depends on several factors: pressure, temperature, and air/water fractions, to name a few. Thus, an appropriate control of the valves requires some experience with the facility. In the case of ramp-up tests, a few pre-tests were necessary to correctly choose the operational ranges.

**Holdup calculation**

The present instrumentation installed in TowerLab does not allow for local holdup measurements. Thus, we consider the average holdup ($\alpha$) to be constant for the entire length of TowerLab. Holdup is calculated by measuring the volume of water inside the test section during a given test ($V_W$) and dividing it by the total volume of the annular space ($V_T$), such that:

$$\alpha = \frac{V_W}{V_T} \tag{44}$$

The total volume of the annular space is known and equal to 0.3406 $m^3$. The volume of water inside the casing at any given moment is measured by the use of the quick-action valve V6 and the pressure measurement from P1V, shown in both Figure 5 and Figure 6 (Validyne DP 15, pressure measurement range varying from 0 to 70 psig and accuracy of 0.25% of full scale – FS). Valve V6 can change from fully open to fully closed in less than one second. Thus, by closing this valve (in a process we refer to as a **shut-in**), we can stop any test after it has reached steady-state and then estimate the amount of water accumulated downstream of valve V6.

As indicated in Figure 6, the test section itself begins on the 1st floor and extends up to the bottom of the 10th floor. This, together with what was explained in the last paragraph, would suggest that valve V6 is found on the 1st floor. However, because of lack of space, this is not the case, and valve V6 had to be installed in the basement, approximately 5-m below the lowest point of the test section. Since estimating the volume of water inside the 2-in. pipeline that connects V6 to the casing (including fittings, valves and unions along it) would be rather imprecise and lead to error, we installed a check valve (VACK) as close to the lowest point on the casing as possible. The presence of this check valve made it possible to minimize errors in measuring the volume of water retained in the test section: once V6 is closed, all the water will be retained downstream of (above) the VACK, which implies that $V_W$ will be kept in the casing and not in the pipes upstream. A minor fraction of $V_W$ actually stays upstream of the entry point of the casing, between the VACK and P1V, and this volume is referred to

as $V_{\min}$ in the calculations. This volume is estimated by using the dimensions of the pipes, resulting in 0.004975 $m^3$, that is, 1.461% of $V_T$.

After shut-in, the water inside the annulus falls and accumulates above the VACK. We calculate the volume inside the facility by measuring the pressure at the bottom of the casing after shut-in with pressure meter P1V. The relation between volume of water and pressure is given by using the flowchart seen in Figure 7, where the variables in the equations presented are explained graphically in Figure 8.

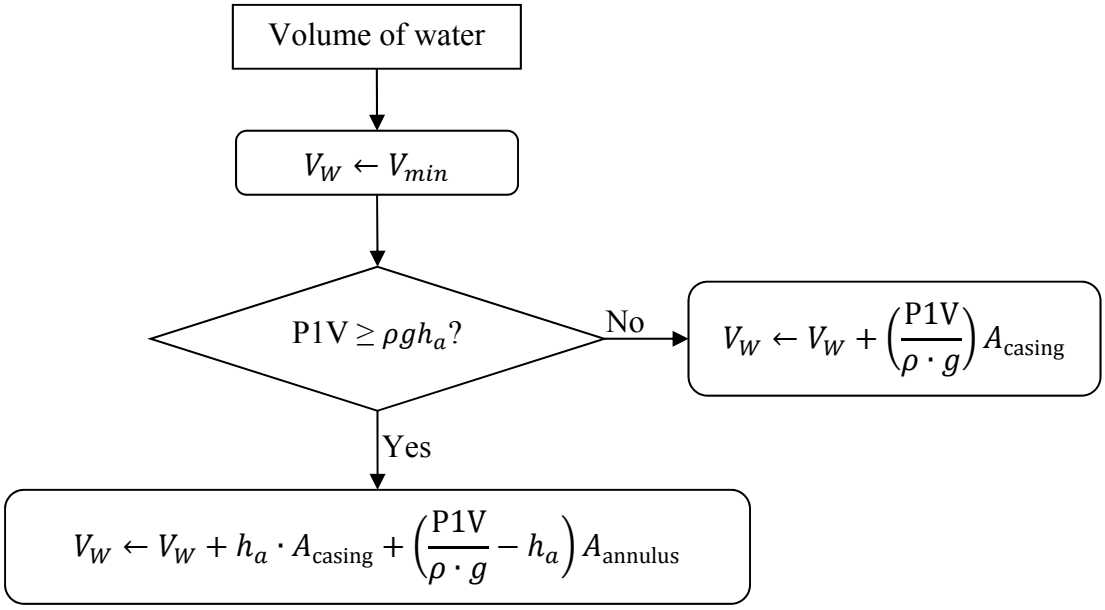


**Figure 7:** Flowchart showing the steps taken to estimate the total volume of water inside TowerLab annulus section after shut-in.

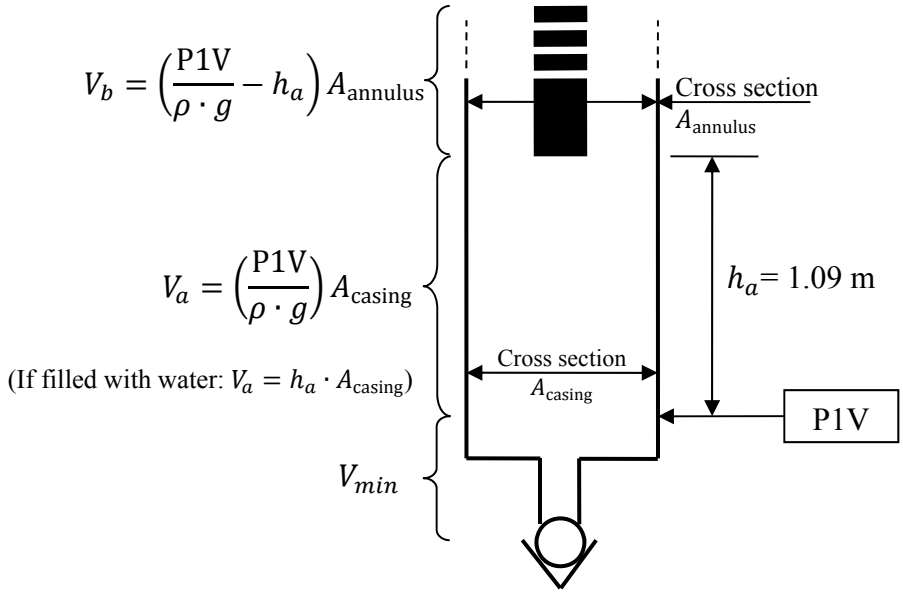


**Figure 8:** Pressure-volume relations at the bottom of the casing.

In these equations, $\rho$ is the density of the tap-water from College Station (997.3 kg/m$^3$, value measured in the lab), $g$ is the acceleration due to gravity (9.81 m/s$^2$), $A_{\text{casing}}$ is 0.01192 m$^2$ and $A_{\text{annulus}}$ is 0.008148 m$^2$.

The accuracy of the measurement is hard to estimate given the way $V_W$ is calculated. We must consider not only possible pressure measurement errors, but also the variations of holdup throughout the test. Furthermore, no test can be exactly reproduced every time. We must see our results as test regions where air and water rates vary within a certain range rather than representing exact points.

That being said, the accuracy of holdup measurement was estimated by checking the real accuracy of the pressure meter P1V. First, we chose five random points to be measured: 0, 20, 40, 50, and 70 psig. Then, using a deadweight machine (standard equipment for calibration of pressure transducers), we recorded the P1V readings for

every point. The order of the data points was picked randomly, with each one being recorded five different times.

After the analysis of the data, we concluded that the average standard deviation when measuring the hydrostatic pressure using P1V is 0.006217 mV. This corresponds to a pressure measurement inaccuracy of 0.09346 psig, which in turn represents a 0.06587-m (2.593-in) column of water, or a volume of 0.0005367 $m^3$. Dividing this volume by $V_T$, we determine the holdup measurement uncertainty to be 0.158%.

**Eccentricity of the tubing in the annular space**

As indicated before, at the top of test section is a structure that holds the tubing in place at a centralized position in relation to the casing. However, the eccentricity of the tubing inside the casing can be controlled by the use of three individual sets of screws (each set referred to as a **positioner**). The locations of the positioners are given by the red arrows shown in Figure 6. A picture of a positioner is presented in Figure 9. Besides the positioners (installed after the start of the project), a centralizer was also placed at the bottom of the tubing, indicated by the red cross at the lower part of the test section in Figure 6. The loose end of the tubing inside the casing represented a safety issue since it would wobble during tests, hit against the acrylic wall, and risk breaking the casing. The location of the bottom tip of the tubing, on the other hand, did not allow for the installation of a positioner. We had to opt to put in place a metal structure that keeps the tubing concentric with the casing at all times.

**Figure 9:** Detail of the positioner with its three screws.

The screws composing one positioner are separated equally around the casing such that by screwing them in and out, we are able to control the position of the tubing inside the casing. The position, however, can only be controlled visually, since we lack of any other way to measure the in-situ distance between the outside wall of the tubing and the inside wall of the casing. For this reason, we only worked with two configurations: concentric, wherein the casing and tubing are concentric, and fully eccentric, wherein tubing touches the casing wall, but only in those regions where there is a coupling between drilling stems. The couplings have an outside diameter (OD)

greater than that of the tubing, which will create a small gap between the drilling stems themselves and the casing.

The green lines in Figure 6 represent the positions of the tubing when concentric (dashed line) and eccentric (bold line). As can be noticed, the eccentricity of the tubing can only be assured between the 2nd-floor positioner and the 8th-floor positioner. Downstream and upstream of this region, the tubing is in transition from concentric to eccentric since it is always centered at the 1st and 10th floors. In general the cross section of the two configurations will look like the schematics shown in Figure 10, where the coupling diameter is exaggerated in relation to the tubing to emphasize the final result.

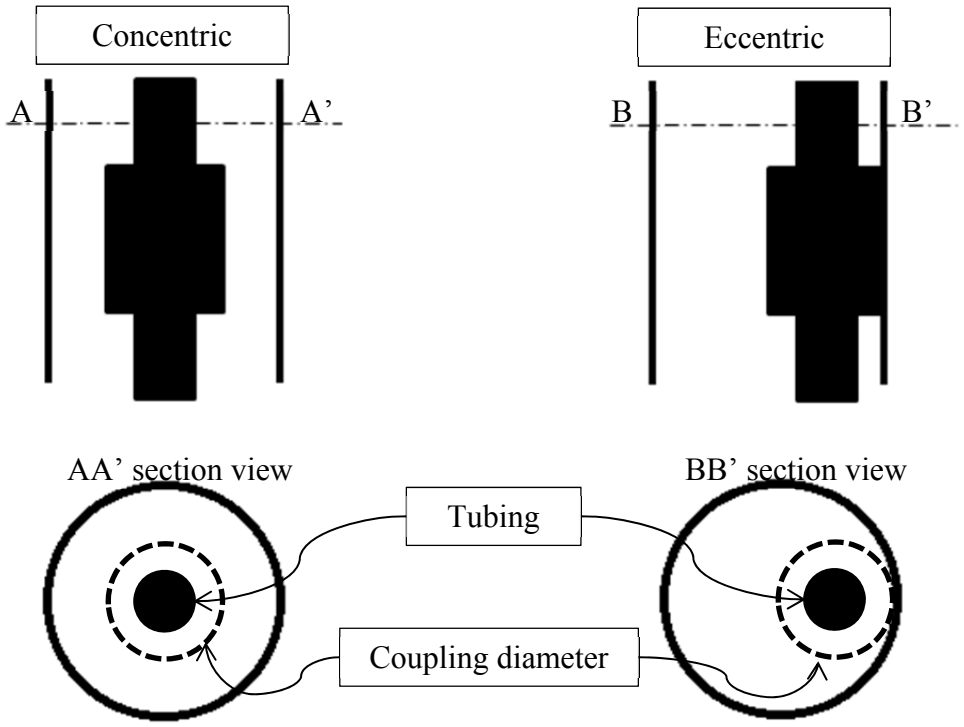


**Figure 10:** Longitudinal and cross section views of the concentric and eccentric configurations.

**Pressure drop measurements**

Figure 6 also shows the location of the pressure meters along the casing. These meters are Validyne model DP 15, with accuracy equal to 0.25% of FS. The pressure transducer at the 3rd floor is referred here as P3 and is calibrated to read from 0 to 80 psig. The pressure meter at the 9th floor is called P9 and can read pressures from 0 to 30 psig. The pressure drop is calculated by the equation below:

$$\Delta p_{39} = \overline{P3} - \overline{P9} \tag{45}$$

where $\overline{P3}$ and $\overline{P9}$ are the average pressures from P3 and P9, respectively. The frequency of measurements is 10 Hz for steady-state and ramp-up tests (3- minute recordings in the first case and up to 30 minutes in the second case). In the hysteresis tests, the frequency of data acquisition was set to 5 Hz to accommodate the length of the recorded data (approximately 80 minutes).

## Building TowerLab operational maps

The first step into the achieving the objectives of this study concerns the characterization of the facility itself. Several steady-state tests were run in concentric and eccentric configurations.

A steady-state test consists of running the experiment at given mass rates of water and air. For each test, a time of approximately 20 minutes is allowed after the water starts going back to the water tank through the return line (see Figure 5). After this period, it is assumed the flow has reached steady-state. In the early stage of the project, the waiting period to reach steady-state varied from 10 to 120 minutes for the same

combination of air and water rates. Since no difference was seen in the results, a 20-minute time was adopted for practical reasons.

Once steady-state has been reached, data is recorded for 3 minutes, at a rate of 10 Hz. While the data is being recorded, videos are taken from the 1st, 4th, 6th, and 8th floors simultaneously for 30 seconds. One additional 5.4-second video is recorded at the 6th floor with a high-speed camera at a rate of 250 frames per second.

After data and videos have been recorded, the experiment is stopped by shutting-in the facility, as explained in the "Operations" Section. After that, a period of at least 15 minutes is given for the water to run down the walls of the casing and tubing to the bottom of the facility, where it accumulates and the pressure P1V is read and stored manually. The 15-minute time is the minimum waiting time for all the water to run down; however, the final reading of P1V is determined only when a variation lower than 0.01 psi/min is verified (which is equivalent to 45 ml/min, or 0.0016 $ft^3$/min).

The data measured during these experiments are:

1. Mass rate of water (from SFWB)
2. Volumetric rate of air (SFAB2) or mass rate of air (SFAB)
3. Air pressure downstream of the air flowmeter (SPAAB)
4. Air temperature downstream of the air flowmeter
5. Pressures at 3rd and 9th floors (P3 and P9, respectively)

P1V and P1R are not used in the pressure drop calculations because they are both located below the tubing's lowest point. From the measurements, we are able to calculate the parameters listed below.

1. Density of air (Eq. 14)
2. Viscosity of air (Eq. 15)
3. Air and water superficial velocities (Eqs. 5 and 6)
4. Reynolds number (Eq. 7)
5. Weber number (Eq. 10)
6. Froude number (Eq. 11)
7. Liquid holdup (Eq. 44)
8. Pressure drop between 3rd and 9th floors (Eq. 45)

The tests were performed in a variety of air and water rate combinations, according to the ranges shown in Table 5. Despite the flexibility of the facility, the majority of tests were focused on intermediate to high air rates and low to intermediate water rates.

**Table 5:** Range of mass rates used to characterize TowerLab.

| Phase | Facility range (kg/h) | Test focus (kg/h) |
|---|---|---|
| Air | 100 – 600 | 350 – 600 |
| Water | 100 – 1400 | 100 – 1,000 |

An eighth parameter is calculated and plotted to evaluate the measurement errors inherent to TowerLab facility. The uncertainty analysis is based on what was presented on Chapter III. In our case, we were interested in studying the measurement errors associated with the pressure drop between the 3$^{rd}$ and 9$^{th}$ floors. Thus, if the pressure drop is:

$$\Delta p_{39} = p_3 - p_9 \tag{46}$$

The uncertainty of this derived property ($u_{39}$) is, from Eq. 35:

$$u_{39} = \sqrt{B_{39}^2 + P_{39}^2} \tag{47}$$

where $B_{39}$ and $P_{39}$ are the bias and precision errors associated with $\Delta p_{39}$.

Only two systematic errors are associated with the measurements made by the Validyne DP 15 pressure transducers. The first one is the inaccuracy specified by the manufacturer: 0.25% of the full scale. From that we have $(B_3)_1 = 0.25\% \cdot 80$ psi and $(B_9)_1 = 0.25\% \cdot 30$ psi, that is, 0.20 and 0.075 psi, respectively. The second source of error is related to calibration. We have verified before that this kind of pressure transducer has an inherent calibration error in the order of 0.10 psi (maximum value), thus $(B_3)_2 = (B_9)_2 = 0.10$ psi.

From Eq. 36, we have:

$$B_3 = \sqrt{0.20^2 + 0.10^2} = 0.224 \text{ psi} \tag{48}$$

$$B_9 = \sqrt{0.075^2 + 0.10^2} = 0.125 \text{ psi} \tag{49}$$

Thus, from Eq. 37, where $r = \Delta p_{39}$, we have:

$$B_{39} = \sqrt{\left((1) \cdot B_3\right)^2 + \left((-1) \cdot B_9\right)^2} = 0.256 \text{ psi} \tag{50}$$

The precision errors, on the other hand, can only be given a numerical value during the analysis of the test results; however, they were computed based on Eq. 38, where $P_r = P_{39}$, $\sigma_r = \sigma_{39}$, that is, the standard deviation of the pressure drop

calculations for each point recorded during one test, and $K$ is the number of points recorded during that test.

## Using OLGA 7 to simulate laboratory experiments

OLGA was used as a tool to predict the total pressure drop and the liquid holdup in both concentric and eccentric cases. The case study was implemented by creating a 36-meter long pipe (which corresponds to the length of the test section from the bottom up to the pressure transducer on the 9$^{th}$ floor, P9) and two independent mass flow sources: one for water and another one for air. As boundary conditions, we have first imposed the air and water mass flow rates corresponding to all the cases tested in the lab, and then by imposing the pressure at the outlet node, which corresponds to the pressure readings from P9. The model described above can be seen schematically in Figure 11 below.

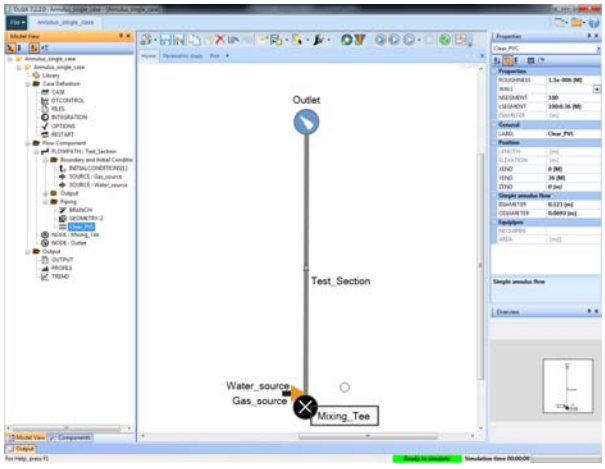


**Figure 11:** OLGA user interface showing the model used to simulate TowerLab experiments.

Once the boundary conditions are set, the program runs its routine to simulate a real time lapse of 720 seconds. This twelve-minute time period was chosen because it has shown to be enough for the numeric model to reach steady-state. After the simulation is concluded, the output file returns the liquid holdup in the annulus and the pressure at the 9-meter height, which corresponds to the pressure transducer in the 3rd floor, P3. The results were average between the 500- and 720-second marks in all cases to avoid any influence from the transient regime.

## Hysteresis

The objective of running hysteresis tests is to verify the effect of past events in the present time. This is achieved by imposing periodic cycles of high and low strain levels. In the present study, the strain imposed to the system is the water mass rate. The rate of water put into the system varies between low to intermediate levels. Meanwhile, the air mass rate is kept constant. The change in water mass rate is governed by square wave cycles of 20-, 15-, and 12-minute periods, each of which has a 10-minute-long high-water-rate period ($\Delta t_h$) followed by a low-water-rate period ($\Delta t_l$) of duration varying between 10, 5, and 2 minutes. Figure 12 illustrates the square waves to which the system is submitted.

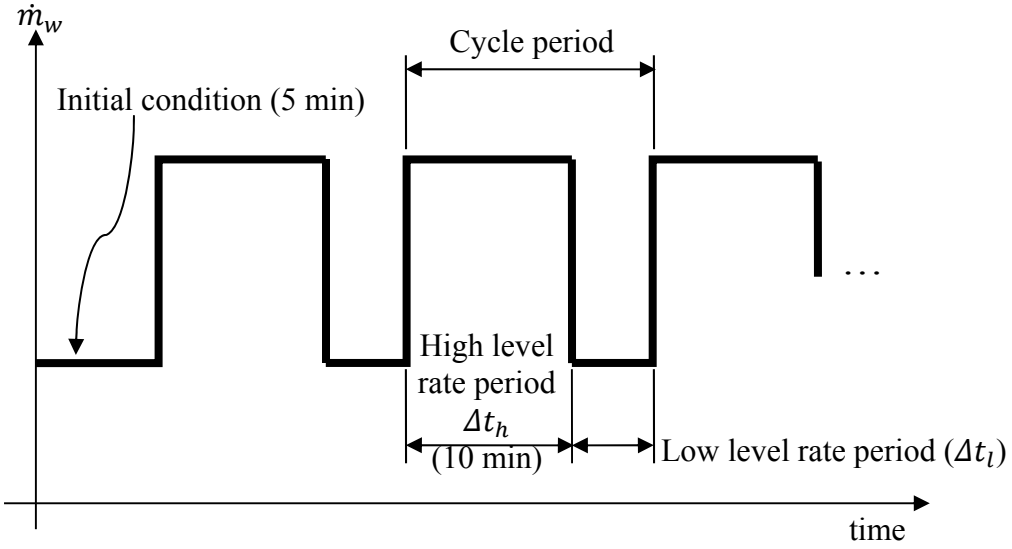


**Figure 12:** Illustration of cyclic square wave between high and low levels of water mass rate during hysteresis tests.

Before the square wave cycles begin, the initial steady-state condition is recorded for 5 minutes. Since holdup measurements cannot be performed without stopping the entire flow, the main analysis focuses on the pressure drop between the 3rd and 9th floors.

The mass rates used in this experiment for both air and water are as indicated in Table 6.

**Table 6:** Test matrix for hysteresis tests.

| Test name | Air rate (kg/h) | Low water rate (kg/h) | High water rate (kg/h) | $\Delta t_h$ (min) | $\Delta t_l$ (min) |
|---|---|---|---|---|---|
| Hysteresis_1 | 600 | 100 | 800 | 10 | 10 |
| Hysteresis_2 | 600 | 100 | 800 | 10 | 5 |
| Hysteresis_3 | 600 | 100 | 800 | 10 | 2 (first cycle: 1) |

### Ramp-ups

In the ramp-up tests, both air and water mass rates change linearly with time from a low-level value (State A) to either intermediate- or high-level values (State B). The low-level rates for water and air are 100 and 200 kg/h, respectively. The intermediate-levels are 600 kg/h (water) and 400 kg/h (air), whereas the high-level values are 1,100 kg/h and 600kg/h for water and air rates respectively. Table 7 below details the three ramp-up tests scenarios used in this study.

**Table 7:** Test matrix of ramp-up tests.

| Test name | State A | State B |
|---|---|---|
| Ramp-up_1 | $\dot{m}_a = 200$ kg/h<br>$\dot{m}_w = 100$ kg/h | $\dot{m}_a = 400$ kg/h<br>$\dot{m}_w = 1{,}100$ kg/h |
| Ramp-up_2 | $\dot{m}_a = 200$ kg/h<br>$\dot{m}_w = 100$ kg/h | $\dot{m}_a = 600$ kg/h<br>$\dot{m}_w = 600$ kg/h |
| Ramp-up_3 | $\dot{m}_a = 200$ kg/h<br>$\dot{m}_w = 100$ kg/h | $\dot{m}_a = 600$ kg/h<br>$\dot{m}_w = 1{,}100$ kg/h |

The change from one level to another happens at a constant rate in a period $\Delta t$. Each ramp-up test is performed at four different times: 20, 60, 120 and 300 seconds. The methodology is explained graphically by Figure 13.

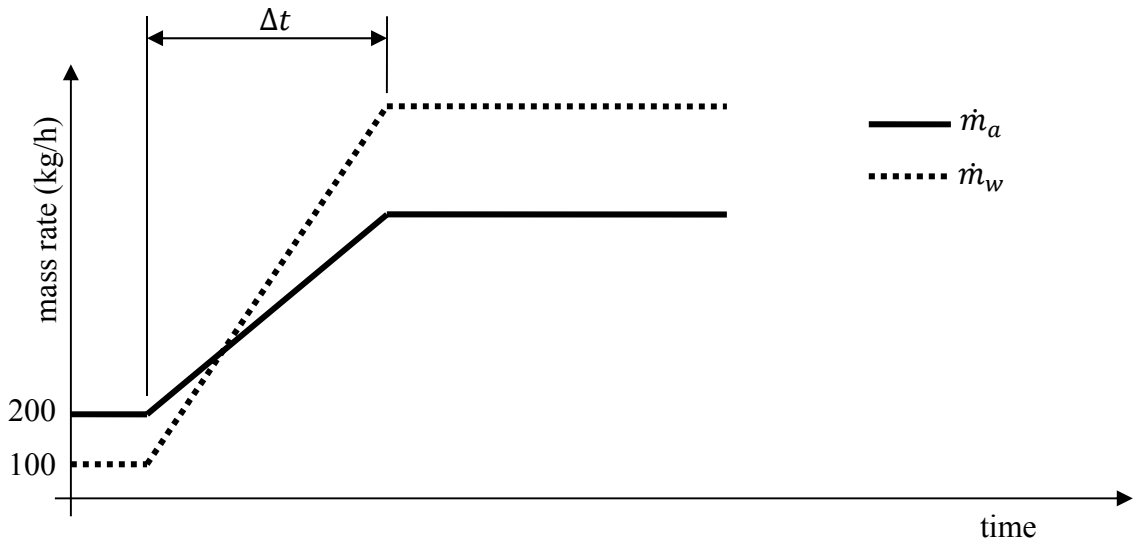


**Figure 13:** Schematic plot of mass rates versus time in ramp-up tests.

As stated in "Holdup calculation" Section, holdup measurements cannot be performed without stopping the flow; thus, the focus of the analysis is also turned into how the pressure drop between 3rd and 9th floor behaves with the changes in air and water rates.

# CHAPTER IV

# RESULTS AND DISCUSSION

In this section we present the results of the tests performed. These results are organized according to the types of tests described in Chapter III.

## TowerLab maps

TowerLab was mapped in both concentric (in a total of 44 tests) and eccentric (34 tests) configurations. The data from the tests are presented in graphical form in Figures 14 through 22. Tables A - 1 and A - 2 in the Appendix contain the numerical values used to plot the graphs in concentric and eccentric cases, respectively.

Figure 14 shows the liquid holdup measurement. The values of holdup are plotted for different combinations of superficial velocities (in ft/sec) and mass rates (in kg/h). Similarly, Figures 15, 16, and 17 show Reynolds, Weber, and Froude number plots. In Figures 14-17 the color scales presented on the right side of the plots correspond, in order, to values of liquid holdup (in %), Reynolds, Weber and Froude. Table 8 compares field and lab ranges for Reynolds, Weber and Froude numbers.

The determination of dimensionless parameters is necessary to characterize the experimental facility and evaluate how it compares to different field geometries. TowerLab is itself a large-scale experimental station when compared to other laboratory facilities, but it may represent just a fraction of the real dimensions seen on the field, especially in deep-water environment. Thus, dimensionless analysis becomes necessary to allow for correctly scaling the liquid and gas flow through the annular space.

**Table 8:** Field values versus TowerLab limits.

| Parameter | Limits | Field values | TowerLab |
|---|---|---|---|
| Reynolds | Min | 1,200,000 | 94,000 |
| | Max | 3,400,000 | 2,100,000 |
| Weber | Min | 41,000 | 5,500 |
| | Max | 260,000 | 73,000 |
| Froude | Min | 5.1 | 14.2 |
| | Max | 31.4 | 186 |

Another parameter calculated from the data acquired is the pressure drop between the 3rd and 9th floors. The pressure drop is plotted for different combinations of superficial velocities and mass rates in Figure 18. A preliminary visual analysis of the data indicates that at intermediate and low gas superficial velocities, the eccentric configuration exhibits higher pressure drops than those seen in the concentric case. The charts in Figure 18 were then plotted again, but now accounting for the errors in measurement and accuracy of the equipment used. The errors were calculated in a worst-case-scenario (WCS) condition, that is, the true value of the pressure drop ($\Delta p_{39}$) is at the border of the 95% confidence interval given by the uncertainty analysis described in Chapter III and Eq. 47. Since we observed that the pressure drop in the eccentric case is higher than that of the concentric, the WCS happens when the concentric case underestimates the real $\Delta p_{39}$ and the eccentric measurements overestimate the real pressure drop. Thus the pressure drops with errors are given as:

$$\left(\Delta p_{39}^{(C)}\right)_{WCS} = \Delta p_{39}^{(C)} + u_{39}^{(C)} \tag{51}$$

$$\left(\Delta p_{39}^{(E)}\right)_{WCS} = \Delta p_{39}^{(E)} - u_{39}^{(E)} \tag{52}$$

where superscripts (C) and (E) indicate the concentric and eccentric cases, respectively.

The plots in Figure 19 were generated using Eqs. 51 and 52. From this Figure, we cannot confirm that the concentric and eccentric configurations will lead to any significant difference in pressure drop measurements since a slight inversion of the trend observed in Figure 18 occurred. This result indicated further investigation was needed, thus, the pressure drop was plotted in a two-dimensional chart using the gas superficial velocity as the governing parameter (x-axis). This resulted in Figure 20, where two separate pressure drop trends can be seen for gas superficial velocities below 20ft/s (beyond this threshold, the pressure drop cannot be differentiated between configurations). The top trend (with triangular markers) corresponds to the eccentric case, whereas the concentric trend is identified by the square markers. The eccentric case trend is always above the concentric one. To confirm that these trends are statistically different, we plotted the graph again in Figure 21, but now included the errors calculated in the worst case scenario.

The inclusion of uncertainty to the graph reveals that the difference between the trends is located very near the 95% confidence interval, making the average values of one case border the uncertainty limit of the other. This statistical analysis, while not perfectly conclusive, is a strong indication that the observed difference in pressure drops between cases is relevant. This is further supported by Figure 22, where the liquid holdup is plotted versus gas superficial velocity, but no difference can be seen between annuli configurations: concentric and eccentric points fall under the same trend and cannot be identified separately.

These observations reveal that the characteristic flow parameter (holdup) for a given gas superficial velocity is independent of the tubing position inside the casing. Nevertheless, for $u_{sg}$ lower than 20 ft/sec, a slight change in pressure loss between configurations indicates that the position of the tubing is the cause of such difference. Further observations, as explained in the next paragraphs, seem to corroborate this hypothesis.

Besides the steady-state tests, 12 other tests in concentric form and 16 in eccentric were performed to characterize the flow regimes seen in TowerLab. These tests were mainly performed within the focus region specified in Table 5 and they were carried out to properly describe, with visual evidence (i.e., videos), how the two-phase flow behaves for different combinations of air and water mass rates. The videos were made manually at the 8$^{th}$ floor of TowerLab. This location was chosen because it is where the last acrylic casing pipe is found. Moreover, the presence of a coupling at eye-level allows for a good visualization of the steady-state flow upstream, downstream and at the coupling. The tests correspond to the summary list seen in Table 9.

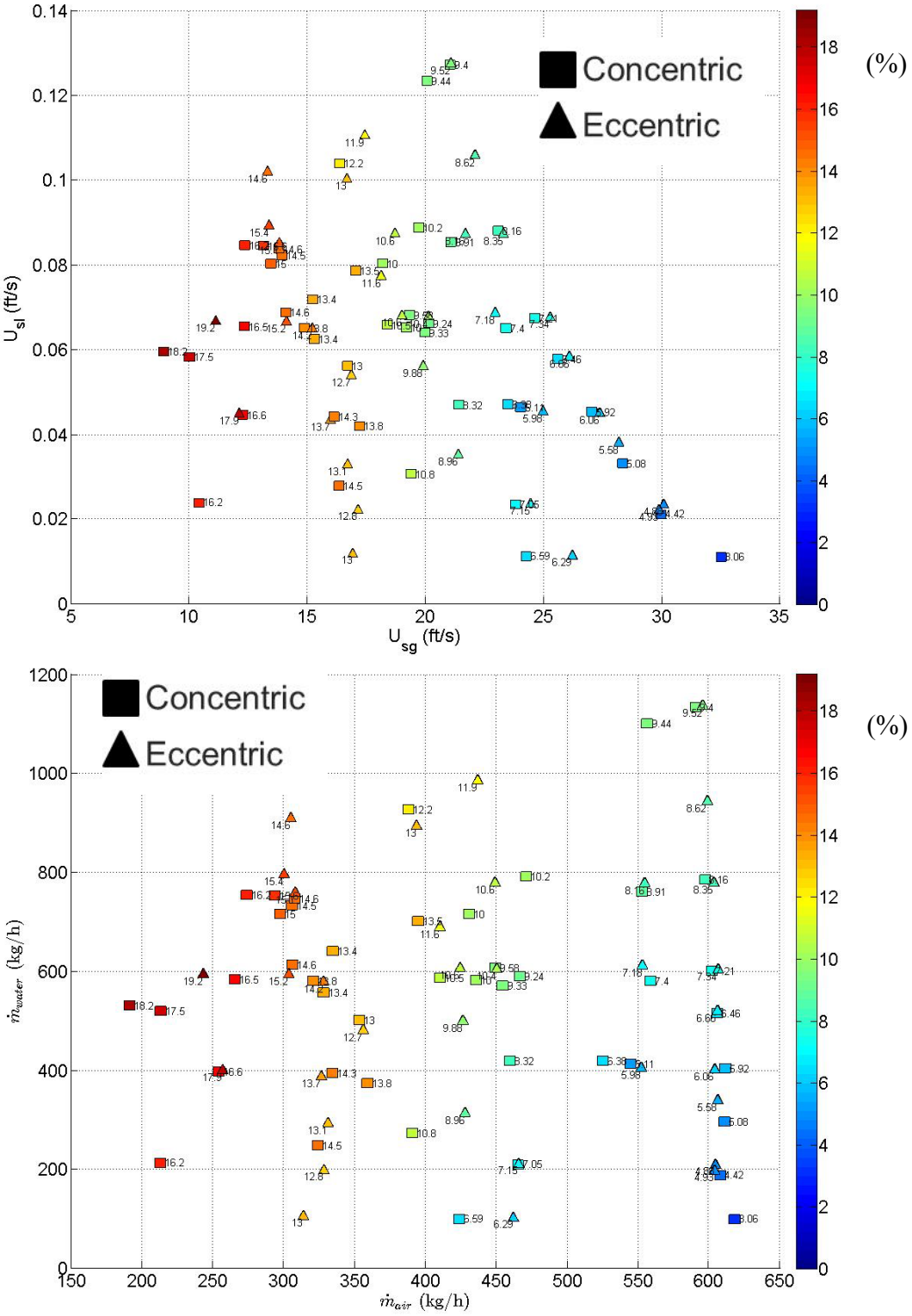


**Figure 14:** Holdup measurements for different combinations of superficial velocities (top) and mass rates (bottom).

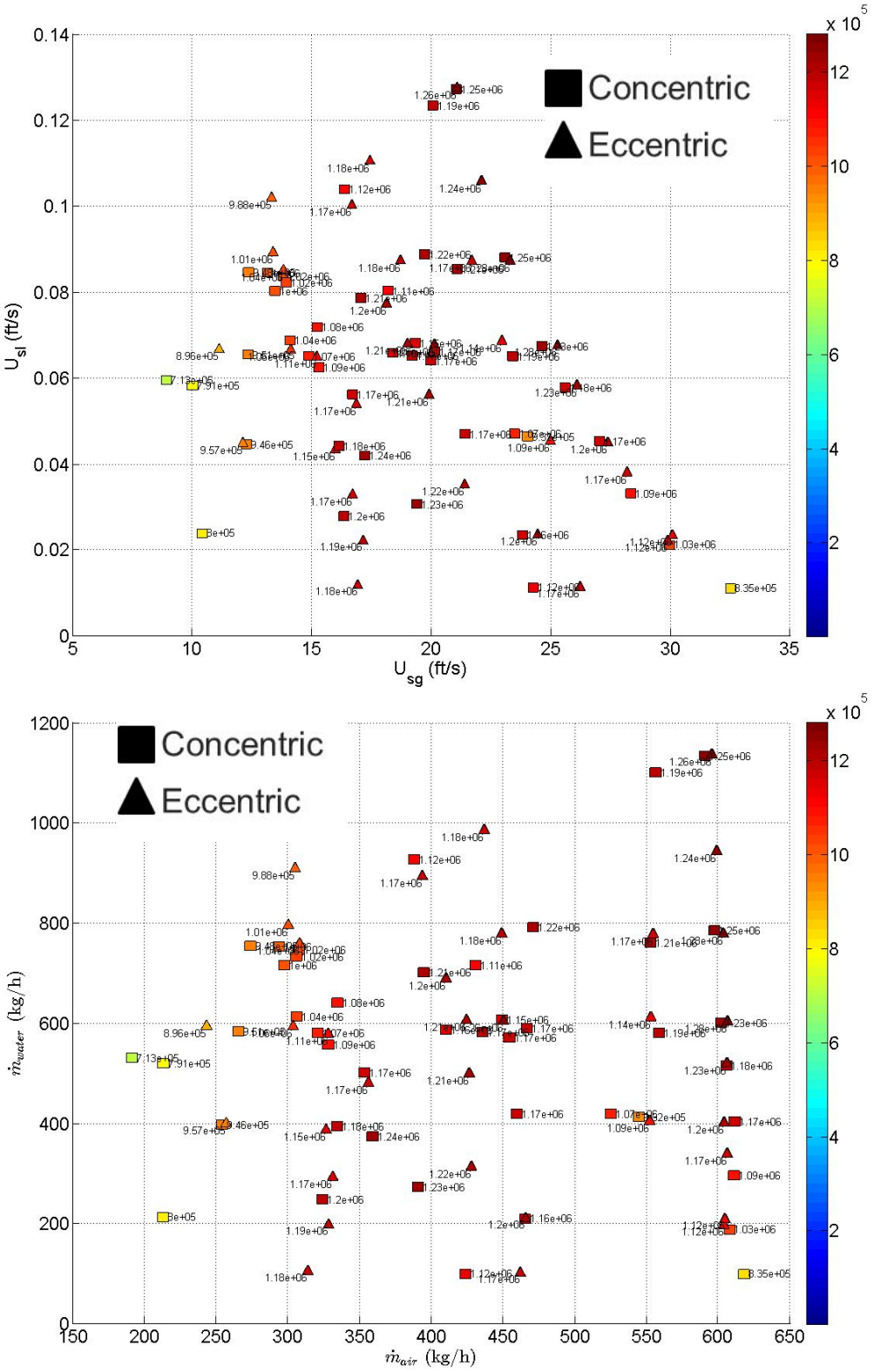


**Figure 15:** Reynolds for different combinations of superficial velocities (top) and mass rates (bottom).

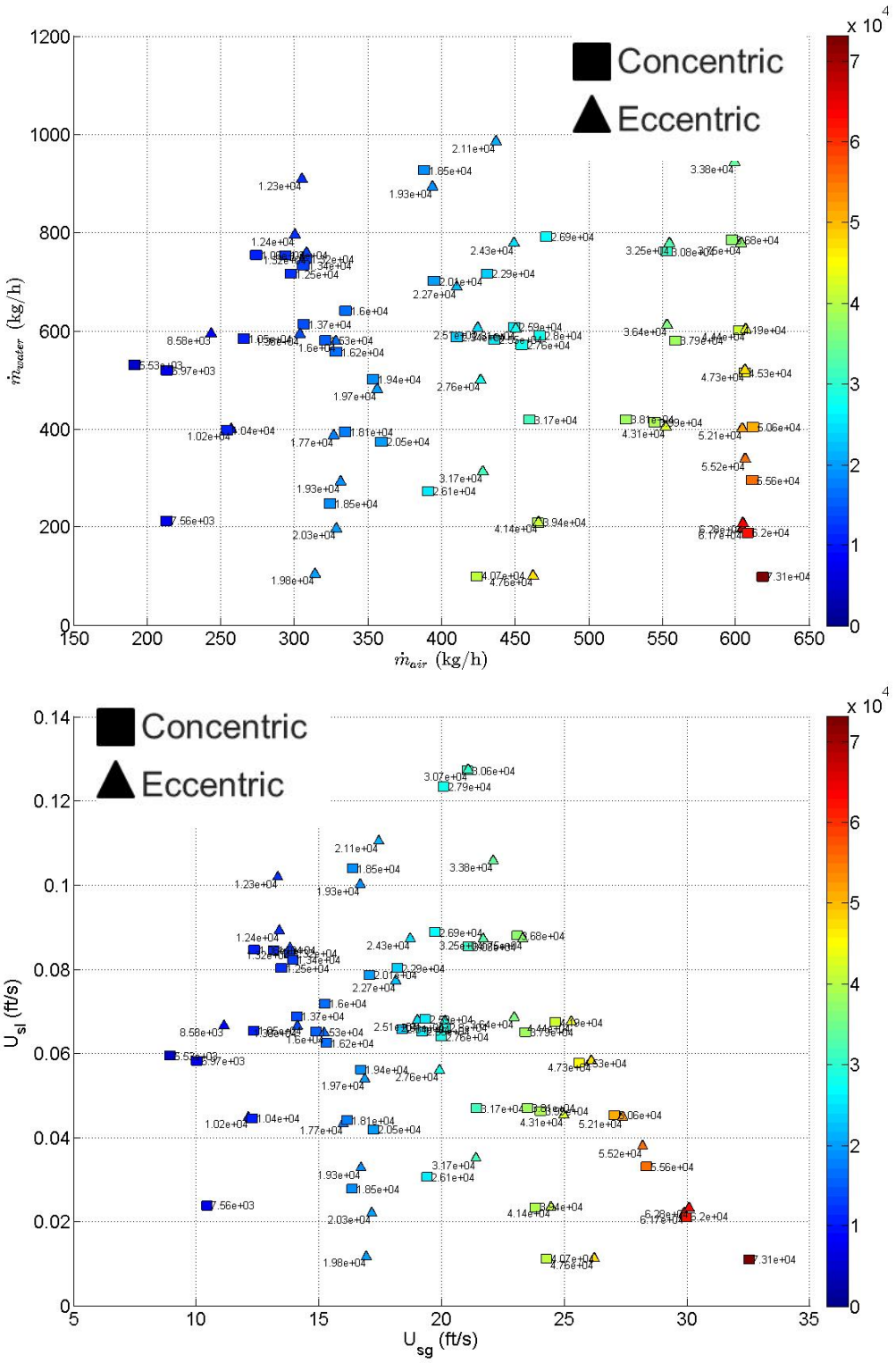


**Figure 16:** Weber for different combinations of superficial velocities (top) and mass rates (bottom).

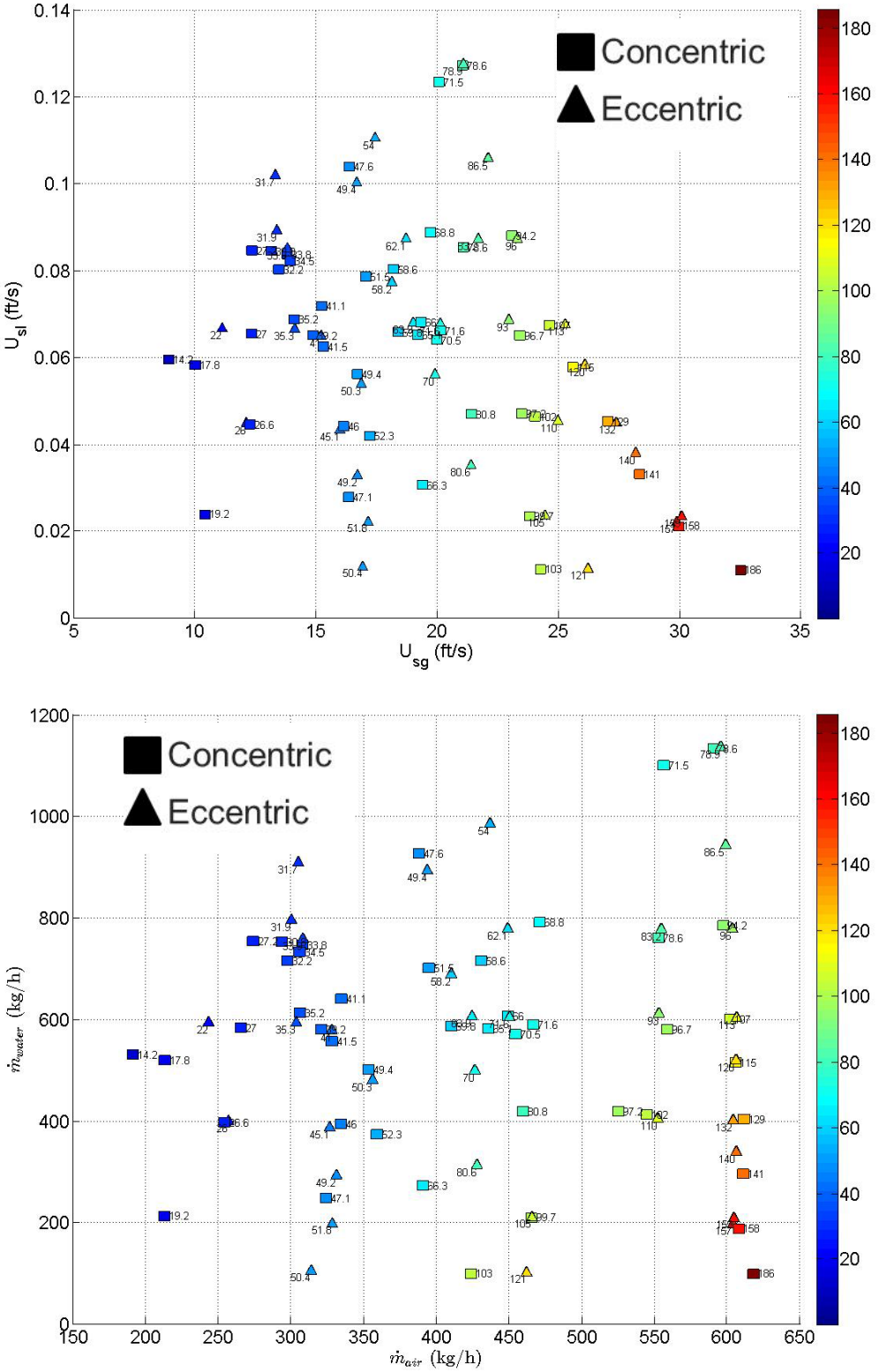


**Figure 17:** Froude for different combinations of superficial velocities (top) and mass rates (bottom).

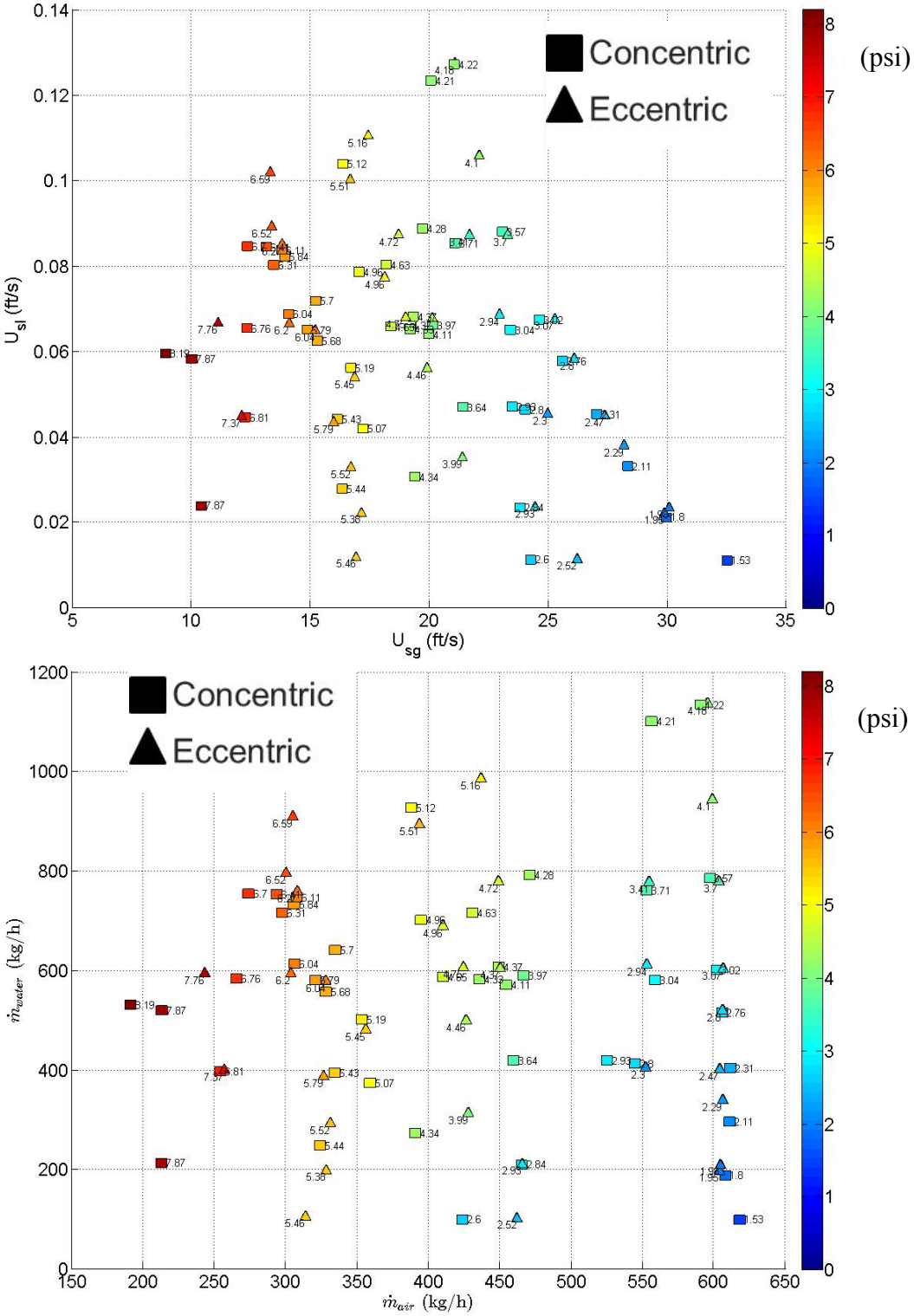


**Figure 18:** Pressure drop between 3rd and 9th floors for different combinations of superficial velocities (top) and mass rates (bottom).

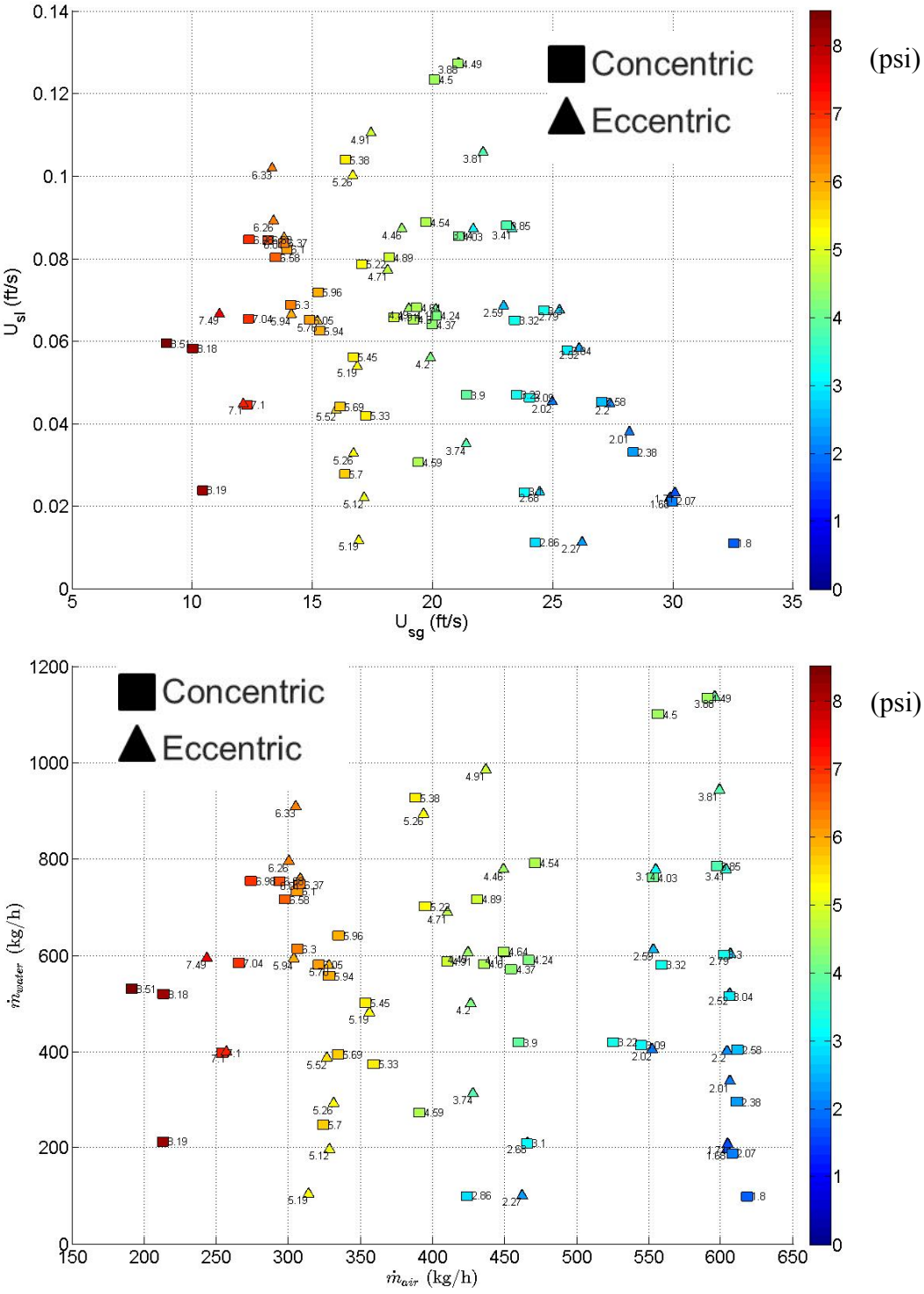


**Figure 19:** Pressure drop between 3rd and 9th floors considering measurement errors and pressure meter accuracy in the worst-case scenario. Plots for different combinations of superficial velocities (top) and mass rates (bottom).

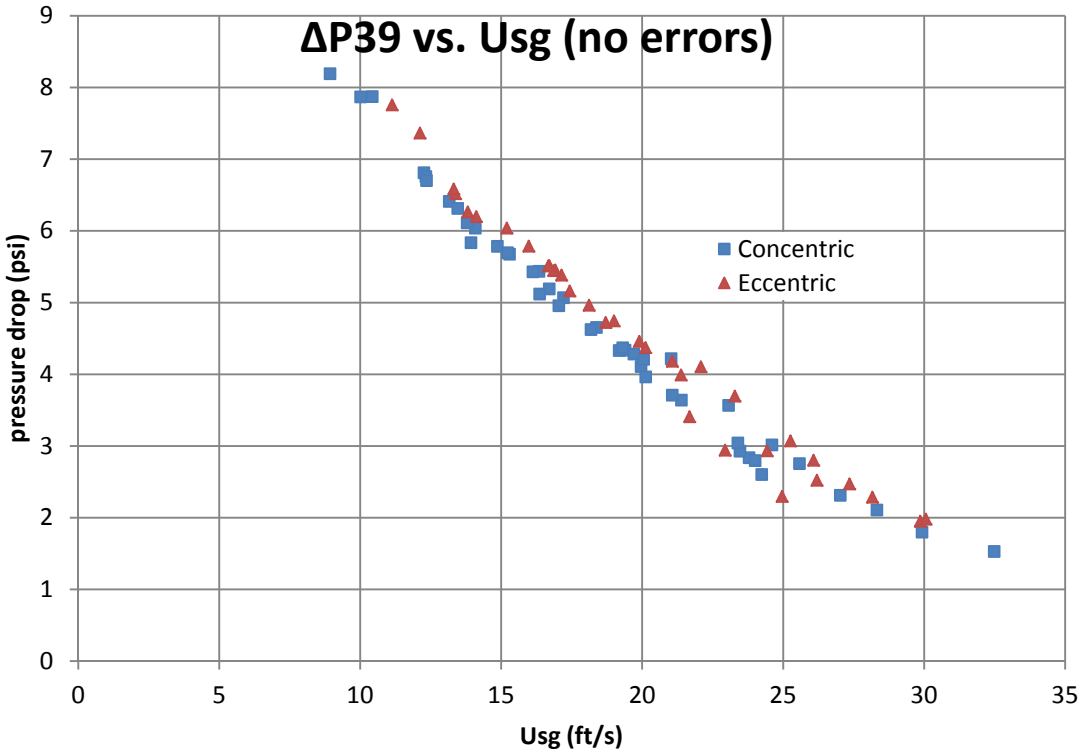


**Figure 20:** Pressure drops versus gas superficial velocity.

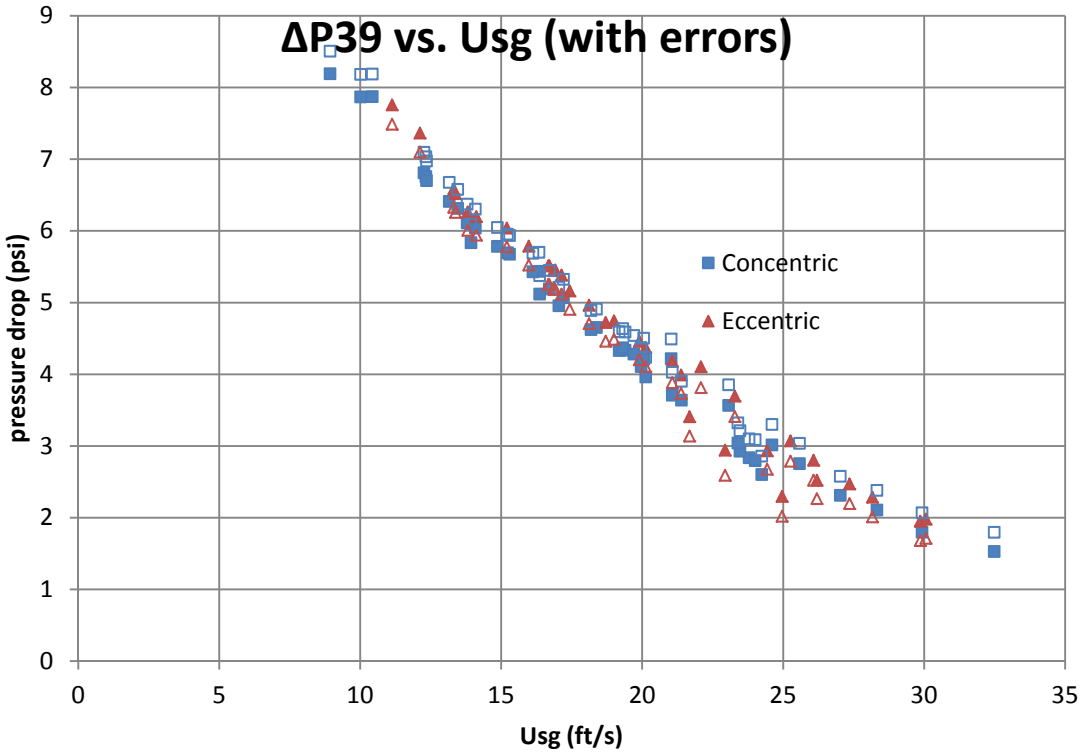


**Figure 21:** Pressure drops with and without errors versus gas superficial velocity.

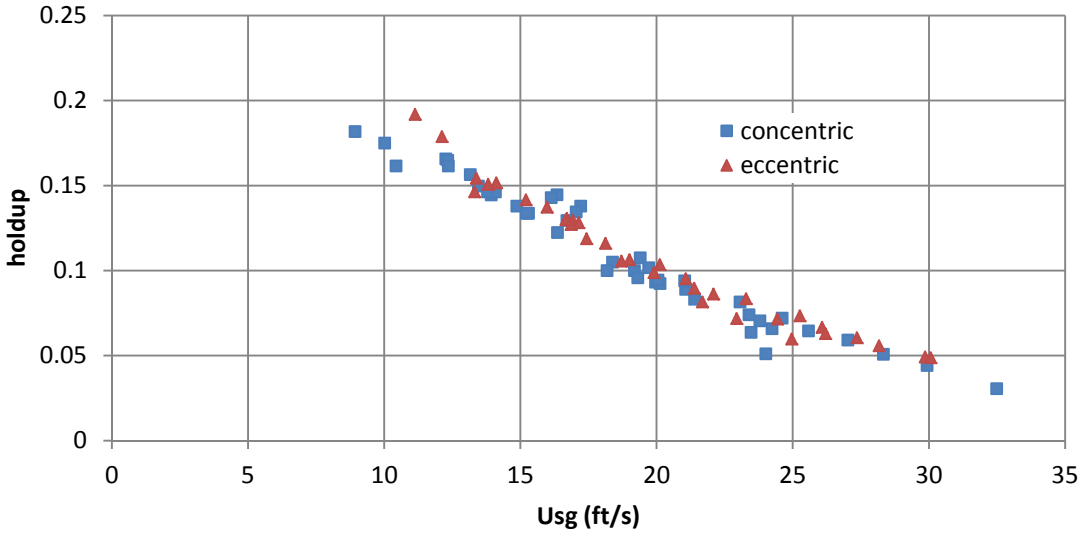


**Figure 22:** Holdup measurements versus gas superficial velocity.

For gas superficial velocities below 20 ft/sec, the liquid distribution around the annulus differs between the concentric and eccentric configurations (Figure 23). Water tends to accumulate in the gap between the tubing and the casing, forcing the air to flow in the larger space that opposes the gap. The water accumulated in the gap recirculates around the couplings, with low upward mobility, characterizing a phenomenon we called **local liquid loading**. The accumulation of water in this pocket is not seen in superficial gas velocities higher than 20 ft/sec; in these cases, the liquid fraction will tend to be located primarily towards the gap, but by no means does the water accumulate locally, as seen before. These two facts are in agreement with the pressure drop difference seen between concentric and eccentric cases, as stated previously. The local pocket of water in the eccentric flow might cause higher pressure losses due to friction, which would explain the trends in pressure drop between concentric and eccentric setups.

Without a mechanistic model, the flow patterns observed in TowerLab can be classified according to a qualitative description of the flow, following the criteria below, shown in order of importance:

1. Film thickness
2. Frequency and volume of disturbance waves (defined below)
3. Similarity to the flow patterns here described

In both concentric and eccentric configurations, churn flow is the most common flow regime seen. At high air and low water rates, we reach a transition region where annular flow may occur at isolated sections of the casing (Zone C1 in Figure 24 and E1 in Figure 25). Zones C2 and E2 are characterized by churn flow with a small number of

high-liquid holdup waves (called here **disturbance waves**) and a thin, but turbulent, liquid film. Zones C3 and E3 are still in the churn flow region, but now disturbance waves are more frequent and a thick liquid film has formed. Zones C4 and E4 are closer to the churn/slug transition zone. In these zones, a thicker liquid film is formed against the casing wall and the disturbance waves are more frequent and bigger in volume. Zone E5 represents the start of the slug region, with big Taylor bubbles being formed. The stability of these bubbles is highly affected by the presence of couplings. Figures 24 and 25 are superimposed for comparison, resulting in Figure 26.

The observations regarding the disturbance waves are in agreement with what is observed in Waltrich et al. (2013). This work was developed for open pipe geometries, measuring and quantifying the waves (referred to as flow structures in the article) in terms of liquid volume and frequency. From this paper we can infer that the frequency on these disturbance waves depend strongly on the gas superficial velocity, which, in turn, is directly related to the mass flow of air. Thus, for lower mass flows, that is, low gas superficial velocities, high-volume, low-frequency wave are expected, whereas for higher air rates, low-volume, high-frequency waves occur. The cited study also makes observations on the behavior of these waves in annular flow; however, this flow regime is not within the range of operation of TowerLab.

**Table 9:** Summary of flow regime characterization tests.

| Tubing setup | $\dot{m}_a$ | $\dot{m}_w$ | $u_{sg}$ | $u_{sl}$ | $\Delta p_{39}$ | Zone |
|---|---|---|---|---|---|---|
| Concentric | 316 | 604 | 19.3 | 0.089 | 5.44 | C4 |
| | 318 | 198 | 22.0 | 0.029 | 4.86 | C3 |
| | 319 | 412 | 20.5 | 0.060 | 5.05 | C3 |
| | 445 | 198 | 30.8 | 0.029 | 3.05 | C1 |
| | 455 | 403 | 28.5 | 0.059 | 3.68 | C2 |
| | 461 | 795 | 25.4 | 0.117 | 4.52 | C3 |
| | 466 | 600 | 27.1 | 0.088 | 4.10 | C3 |
| | 605 | 1094 | 28.1 | 0.160 | 4.07 | C3 |
| | 609 | 598 | 32.5 | 0.088 | 2.99 | C2 |
| | 611 | 215 | 38.8 | 0.032 | 1.84 | C1 |
| | 612 | 788 | 30.7 | 0.116 | 3.47 | C3 |
| | 614 | 402 | 35.5 | 0.059 | 2.43 | C1 |
| Eccentric | 95 | 206 | 4.8 | 0.030 | 13.39 | E5 |
| | 95 | 822 | 4.6 | 0.121 | 13.19 | E5 |
| | 95 | 1150 | 4.6 | 0.169 | 13.40 | E5 |
| | 300 | 196 | 20.2 | 0.029 | 5.85 | E3 |
| | 302 | 592 | 18.4 | 0.087 | 6.21 | E4 |
| | 305 | 1045 | 17.1 | 0.153 | 7.15 | E5 |
| | 307 | 411 | 19.5 | 0.060 | 6.01 | E4 |
| | 444 | 214 | 30.6 | 0.031 | 3.28 | E2 |
| | 448 | 593 | 26.2 | 0.087 | 4.36 | E3 |
| | 457 | 410 | 28.6 | 0.060 | 3.84 | E2 |
| | 457 | 788 | 25.2 | 0.116 | 4.76 | E3 |
| | 598 | 1143 | 27.7 | 0.168 | 4.18 | E3 |
| | 602 | 612 | 32.4 | 0.090 | 2.76 | E2 |
| | 603 | 800 | 30.4 | 0.117 | 3.39 | E3 |
| | 605 | 198 | 39.3 | 0.029 | 1.68 | E1 |
| | 607 | 408 | 35.6 | 0.060 | 2.16 | E1 |


**Figure 23:** Liquid distribution around the annulus in concentric and eccentric positions.

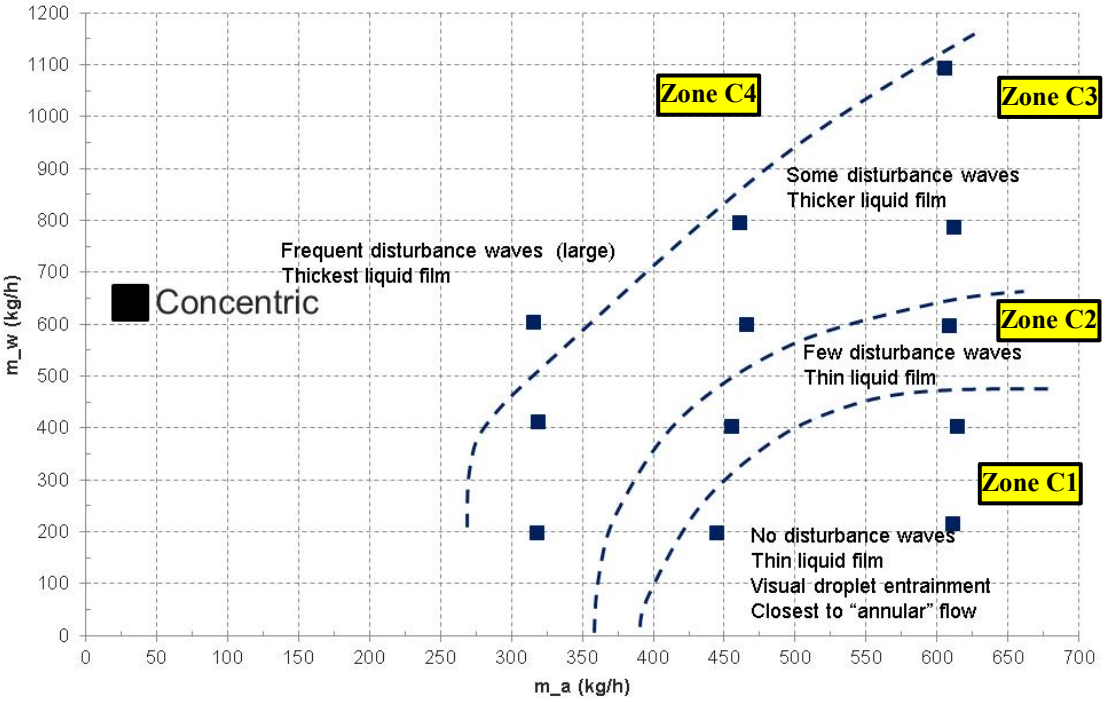


**Figure 24:** Flow regime map for concentric configuration.

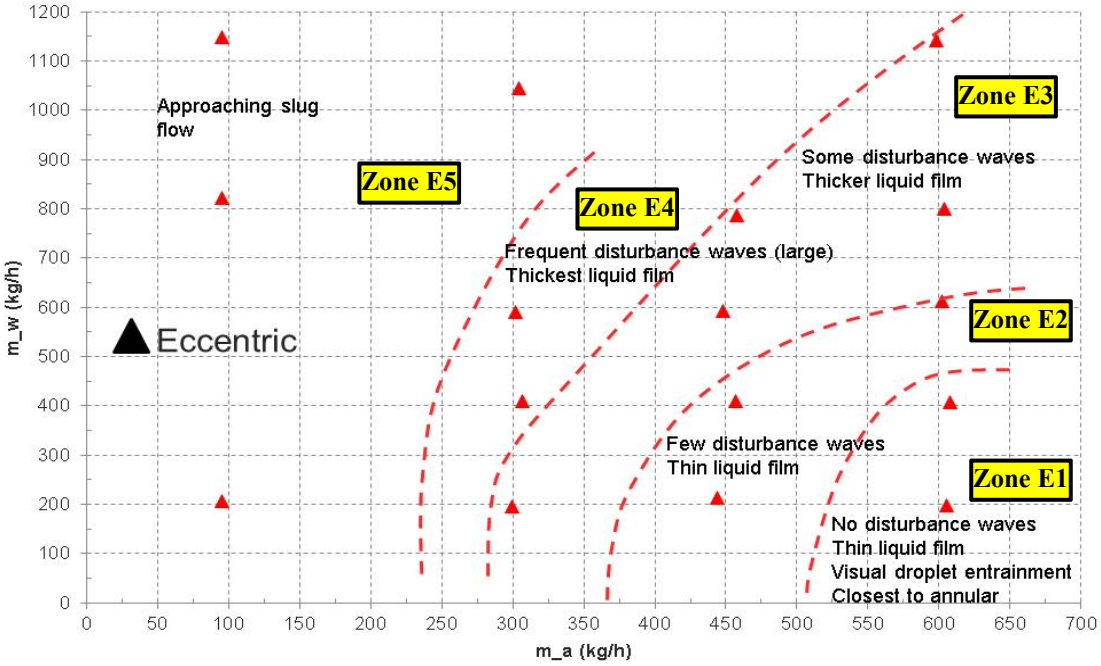


**Figure 25:** Flow regime map for fully eccentric configuration.

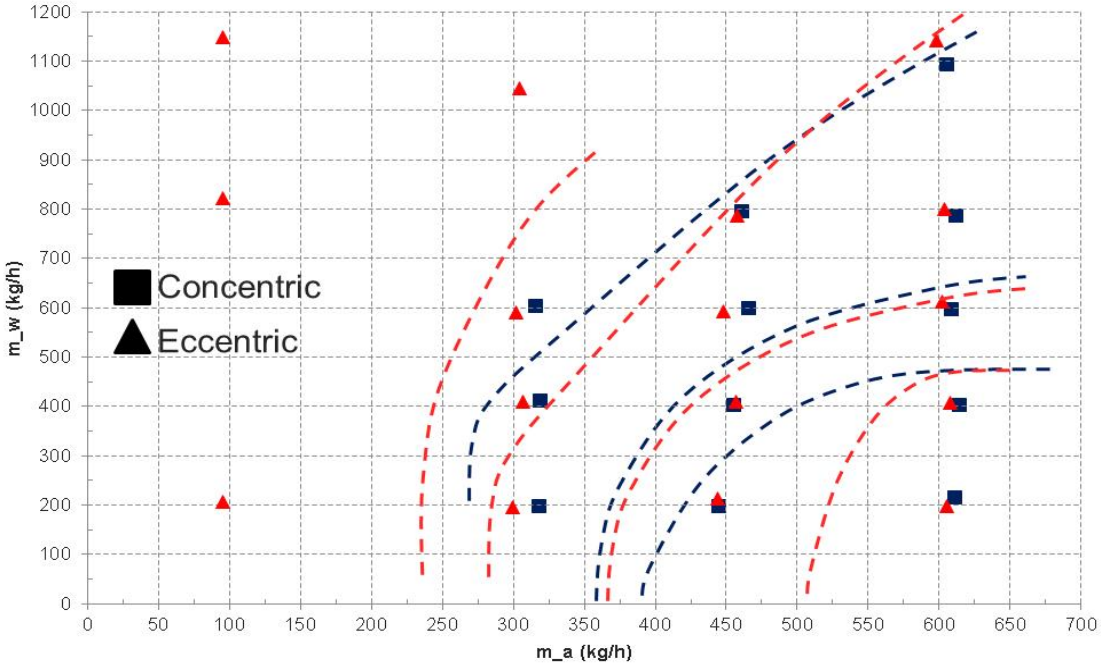


**Figure 26:** Superposition of concentric and eccentric flow regime maps.

## Hysteresis

The hysteresis test results are presented in Figure 27, where the graph on the top corresponds to Hysteresis_1, the middle one is Hysteresis_2, and the one on the bottom is Hysteresis_3. As explained before, the objective of this test is to check if past events caused by the change of a given parameter will affect the future response of the system. In practical terms, hysteresis will indicate whether or not dissipation of energy occurs during the cycles to which the system is submitted. In our study case, if the system were to "lose energy," it would be reflected as an increase in the pressure drop. The dissipated energy is cumulative, adding to itself at each cycle, and it should take place until the system reaches an equilibrium (any further change will not interfere in the behavior of the system) or it fails. That being said, it is expected that TowerLab behaves in either of the following patterns: it is not affected by the change in water mass rates ($\dot{m}_w$); or pressure drop stays constant at the high-water-rate part of the cycle, but it increases at each cycle when we are in the low-water-rate regime. This increase in pressure drop will take place until equilibrium is reached or until it reaches the same value as the pressure drop for the high-water-rate condition. System failure is not considered since it does not have any physical meaning for TowerLab.

The test results presented in Figure 27 clearly show that no increase in pressure drop happens as a function of time. Hysteresis_1 (top plot) shows that, if given enough time, the system will recover to the initial steady state, but, most importantly, it shows that when changing from high $\dot{m}_w$ to low $\dot{m}_w$, the pressure drop will follow the same exponential trend every time. Tests Hysteresis_2 (middle plot) and Hysteresis_3 (bottom

plot) were performed to prove this statement. Even if the system is allowed small times to recover, the change in mass rates will have no effect on the next cycle. Notice that the pressure drop always falls to the same level as it was in the cycles before. In Hysteresis_3, the low $\dot{m}_w$ period in the first cycle is only 1 minute long, whereas the following are 2 minutes long and, even in those circumstances, no pressure loss increase was seen.

Figure 28 shows how TowerLab behaves if submitted to an extreme condition where the changes between high and low water mass rates occur in 30-second cycles. As can be seen, the pressure drop will reach its maximum value after a few cycles. From that moment on, the changes in $\dot{m}_w$ will make the pressure drop oscillate, but it is always limited to a maximum and a minimum. Figure 29 is just another way of looking into the hysteresis test. We can see that the first couple of cycles correspond to a change in pressure drop from 1.5 to 2.0 psig and, after that, the system enters in a cyclic flow state that is represented by the blue ellipse. If any energy loss was taking place, the ellipse-like shape seen in the plot would get narrower until it would eventually fall into a straight line.

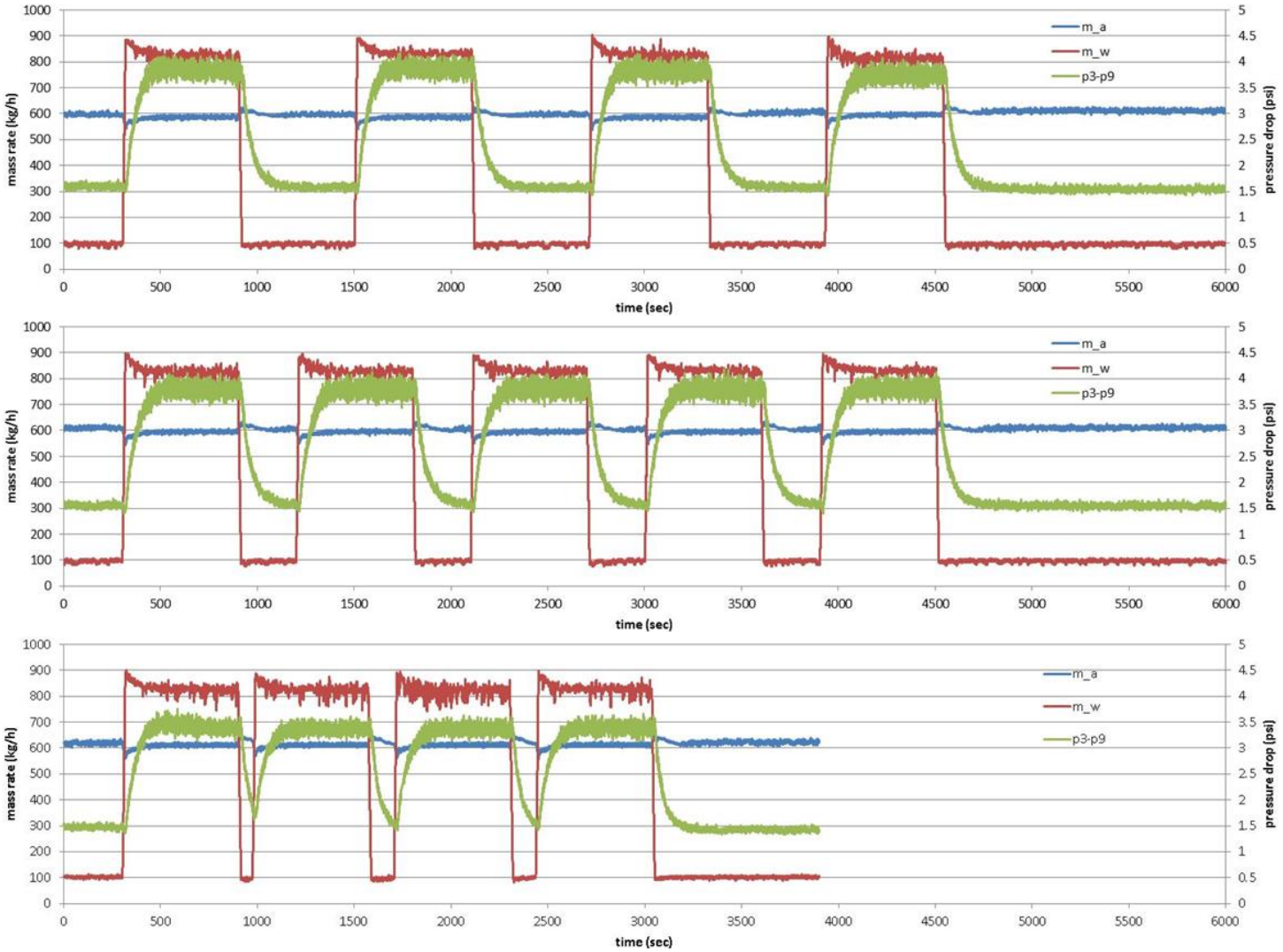


**Figure 27:** Hysteresis tests with low air rate periods of 10 (top), 5 (middle), and 2 (bottom) minutes.

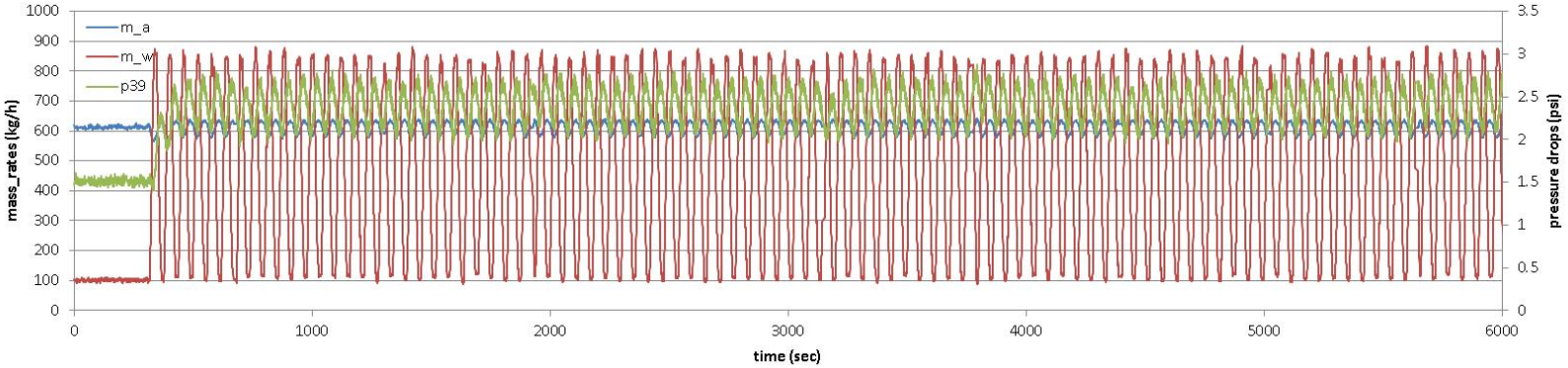


**Figure 28:** TowerLab behavior when submitted to several cycles of water mass rate change.

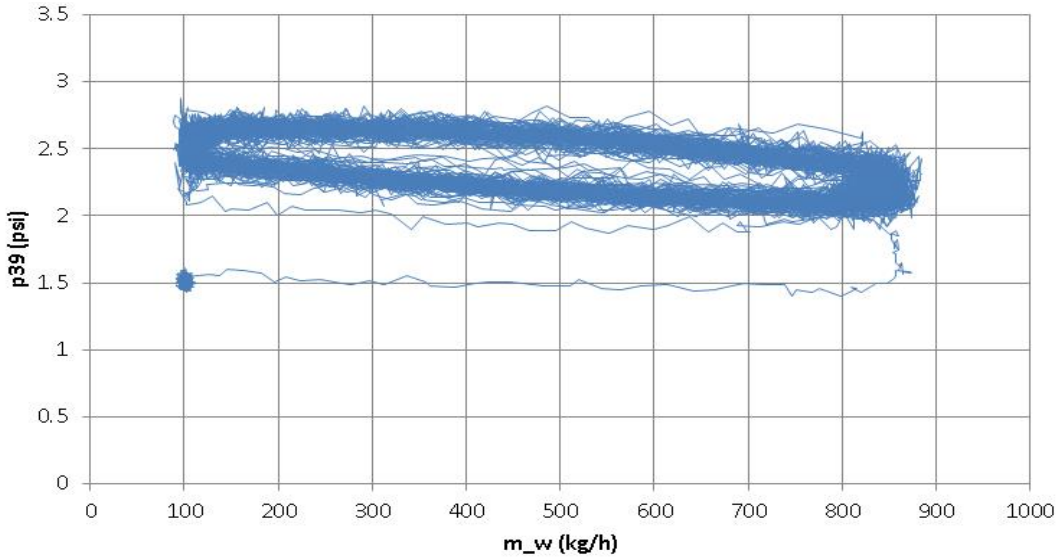


**Figure 29:** Hysteresis analysis showing no change in behavior with cycles.

**Ramp-up**

The ramp-up tests were performed in three different sets as presented in Table 7. Valve opening periods of 20, 60, 120, and 300 seconds were imposed to the system as the control parameters of the mass-rate slopes. The results of these experiments are shown in Figures 30 through 32. Each figure is composed of three different graphs: the one on top is the air mass rate versus time, the one in the middle is the water mass rate versus time, and the bottom plot is the pressure difference between pressure measurements made in the 3rd and 9th floors. All ramps start after 120 seconds, and each test is left running for 10 more minutes after the mass rates have reached their target.

In Figure 30, the ramps do not all start at 120 seconds. The purple curves in the air and water mass rate plots, for example (Ramp-up_1_300s), have their slopes starting beyond 120 seconds and, in the air mass rate plot, the slope is not constant. These reflect the sensitivity of the valve-controlling transducers that do not respond appropriately for small increments. However, despite the appearance of the plots all tests have started at 120 seconds.

The middle plots in Figures 31 and 32 show a surge of air that goes beyond the targeted 600 kg/h in all curves, but with different amplitudes. This surge of air is caused by the way the air compressor behaves and cannot be avoided without further modification of TowerLab physical installations together with the incorporation of a more sophisticated controlling routine.

The results obtained from these experiments are the pressure drop plots seen at the bottom of those pictures. These plots show how the pressure difference ($\Delta p$)

decreases as more water and more air are put into the system. The spikes seen in those plots at the beginning of each test (120 seconds) are the most interesting aspect of the charts. These spikes can be seen in all three figures and their amplitudes seem to depend on only one variable: the ramp slope (also referred to here as the **valve-opening time**, or simply **opening time**).

It could be argued that the spikes in $\Delta p$ are due to the surge of air into the system, but what Figures 31 and 32 reveal is that curves like the ones in blue (20-second period) and in red (60-second period) with similar surge maximums (1,000 and 975 kg/h, respectively) have significantly different responses in their resulting $\Delta p$. The spikes seen in Figures 31 and 32 bottom plots represent an increase of approximately 100% in the pressure drop for the blue curve, whereas for the red curves, the spikes represent only 37.5% of the initial steady-state condition. These spike intensities decrease even more for the opening time of 120 seconds (approximately 25%) and looks nonexistent or negligible for the opening time of 300 seconds. This last observation can also be used to defend the argument that the air surges do not cause the spikes in the $\Delta p$ plots.

The observations made so far are also applicable to the corresponding graph in Figure 30, but they are not as pronounced. The existence of these spikes may be explained by the sudden influx of liquid which is pushed upward by the high rate of air. Since it takes a while for the liquid to climb from the 3$^{rd}$ to the 9$^{th}$ floor, we see the spikes happening shortly after the opening of the valves. As the opening time increases, lesser amounts of liquids are put into the system, and then a lower pressure drop is seen.

A second remarkable feature in the $\Delta p$ plots is the concave part of the curves seen in Figures 31 and 32 just before the equilibrium at steady-state. Contrary to the $\Delta p$ spikes, this part of the curve is not uniquely related to the ramp slope, but it is also linked to the air surge. In all cases, the minimum in the $\Delta p$ curve takes place approximately 50 seconds after the peak in air surge.

Also, the lower the pressure drop minimum, the larger the opening time is. This may be explained by the pressure losses during acceleration of the liquid phase. When large amounts of liquid and gas are thrown into TowerLab, a higher amount of energy is lost at an earlier time because of the variation of liquid velocity. Thus, higher air surges indicate higher amounts of air put into the system, which in turn accelerate the liquid to higher velocities, causing higher energy losses. Kinetic energy losses are generally considered negligible in pressure-gradient calculations, but in transient flow, they must be taken into account.

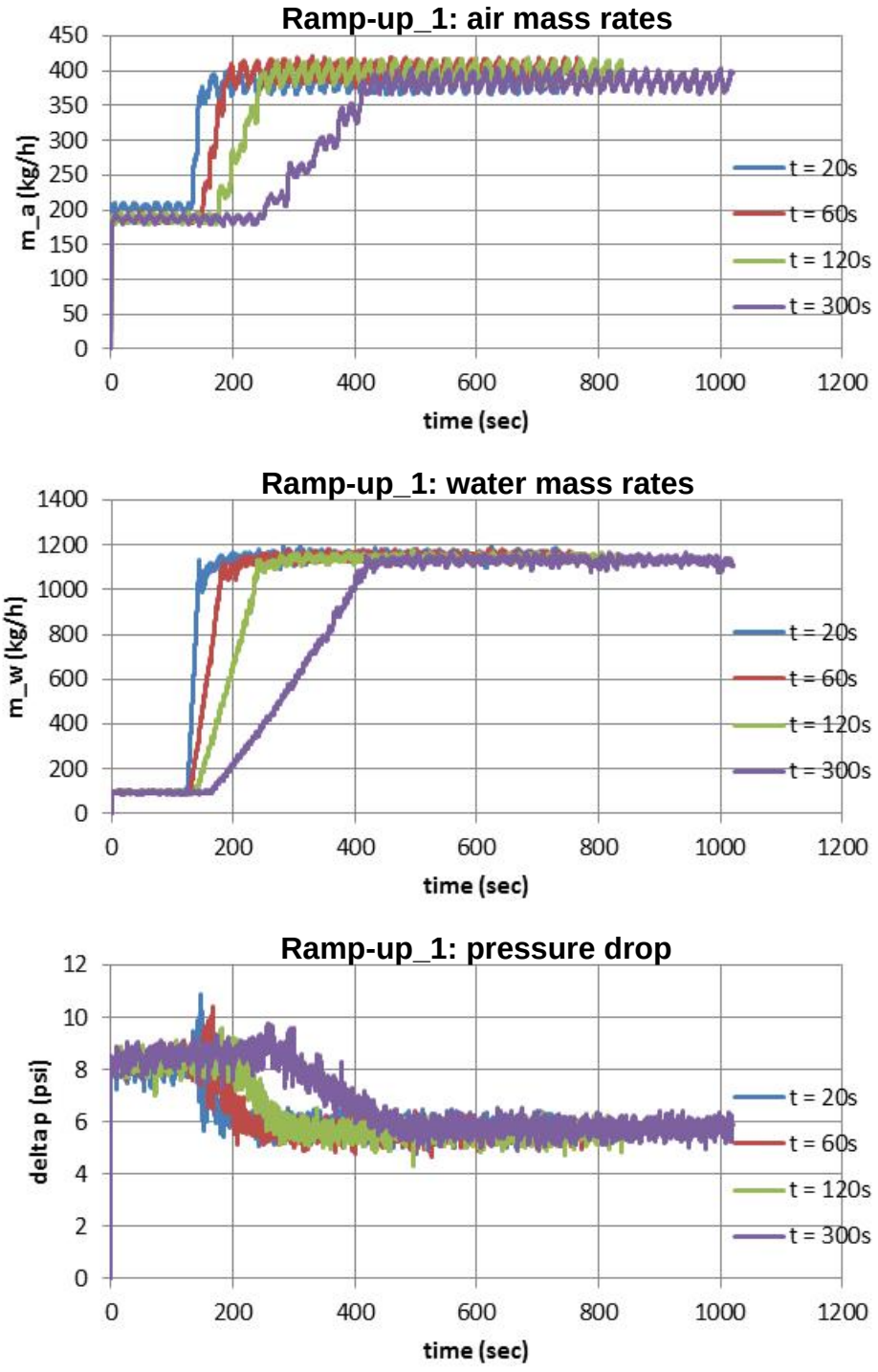


**Figure 30:** Air (top) and water (middle) mass rates, and pressure drop versus time for Ramp-up_1 test.

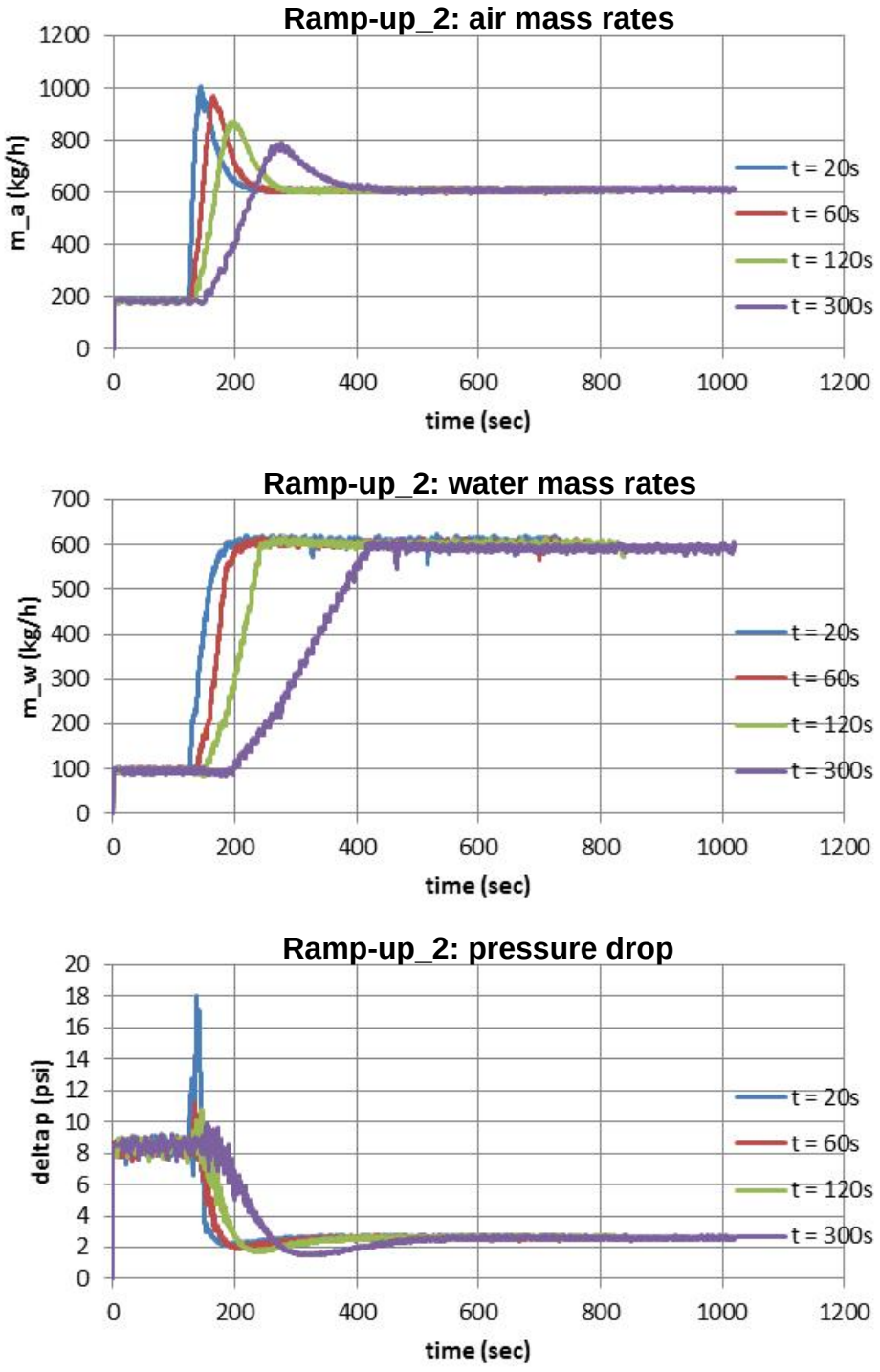


**Figure 31:** Air (top) and water (middle) mass rates, and pressure drop versus time for Ramp-up_2 test.

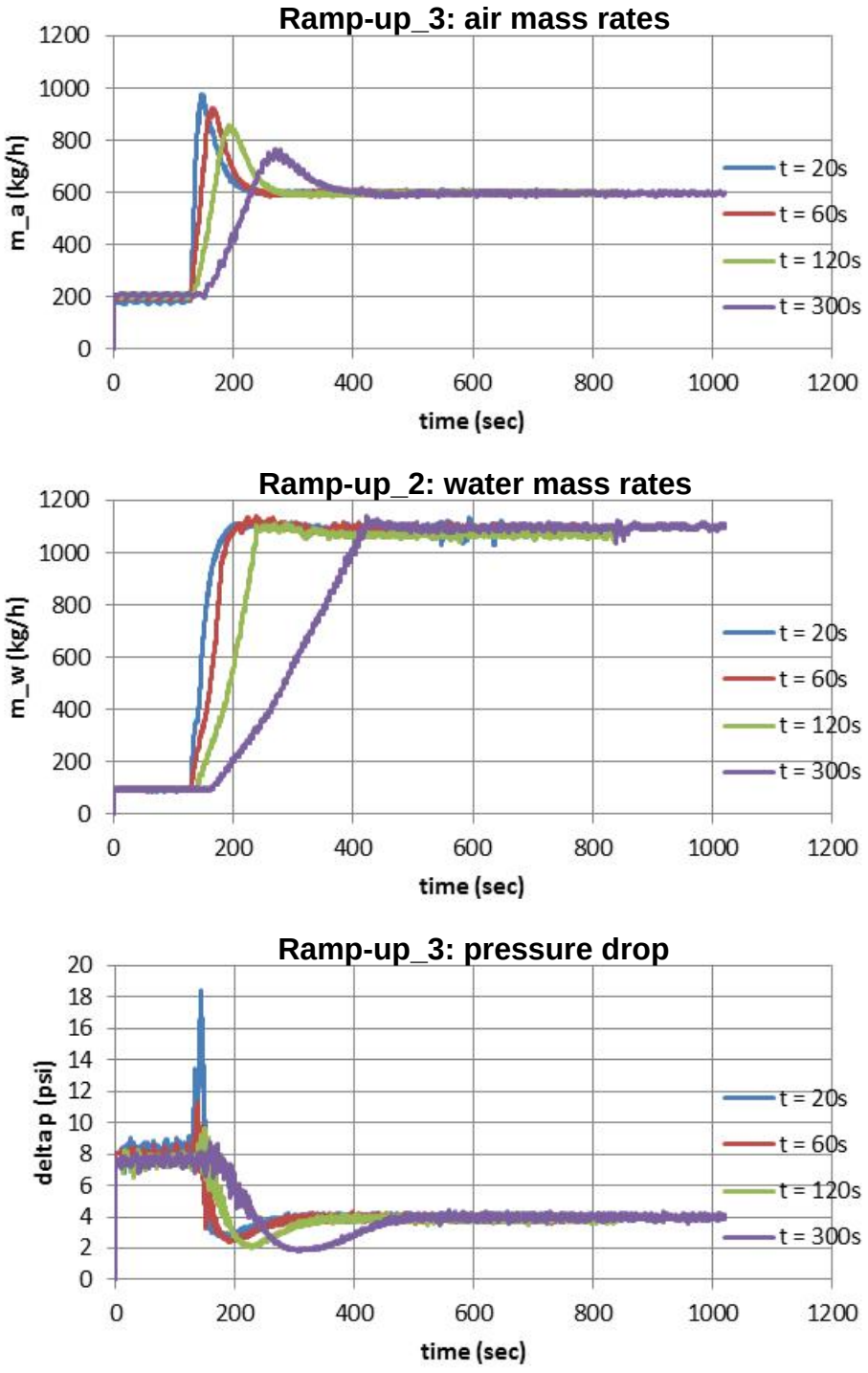


**Figure 32:** Air (top) and water (middle) mass rates, and pressure drop versus time for Ramp-up_3 test.

# CHAPTER V

# PRESSURE GRADIENT PREDICTION

In this section we are interested in applying mechanical principles (based on Eq. 25), and computer based simulations (run on OLGA 7) to predict the results shown in Chapter IV.

## Mechanical analysis

Equation 25 can be rewritten in terms of variables given by the system. Furthermore, if we divide the whole expression by the length between the pressure transducers in the 3rd and 9th floor, we have:

$$\bar{\rho} = \frac{1}{9.81}\left(\frac{\overline{P3} - \overline{P9}}{35.7 - 8.7} + \frac{f \cdot u_{sg}^2}{2 \cdot 0.05390}\right) \tag{53}$$

As stated before, the gas superficial velocity is computed from Eq. 5, the friction factor, from Eq. 26, and $\overline{P3}$ and $\overline{P9}$ are measured. With this equation, we estimate the density of the mix, which in turn is related to the liquid holdup by Eq. 9. Since the densities of the liquid and the gas phases are known, we compute:

$$\alpha_{\text{mech}} = \frac{\bar{\rho} - \rho_g}{\rho_l - \rho_g} \tag{54}$$

We, then, computed the ratio of holdup obtained from Eq. 54 over that measured in TowerLab to assess the accuracy of the analysis. We plot the results against the gas superficial velocity and obtain Figure 33, where on top are the ratios for the concentric case and on the bottom those for the eccentric configuration.

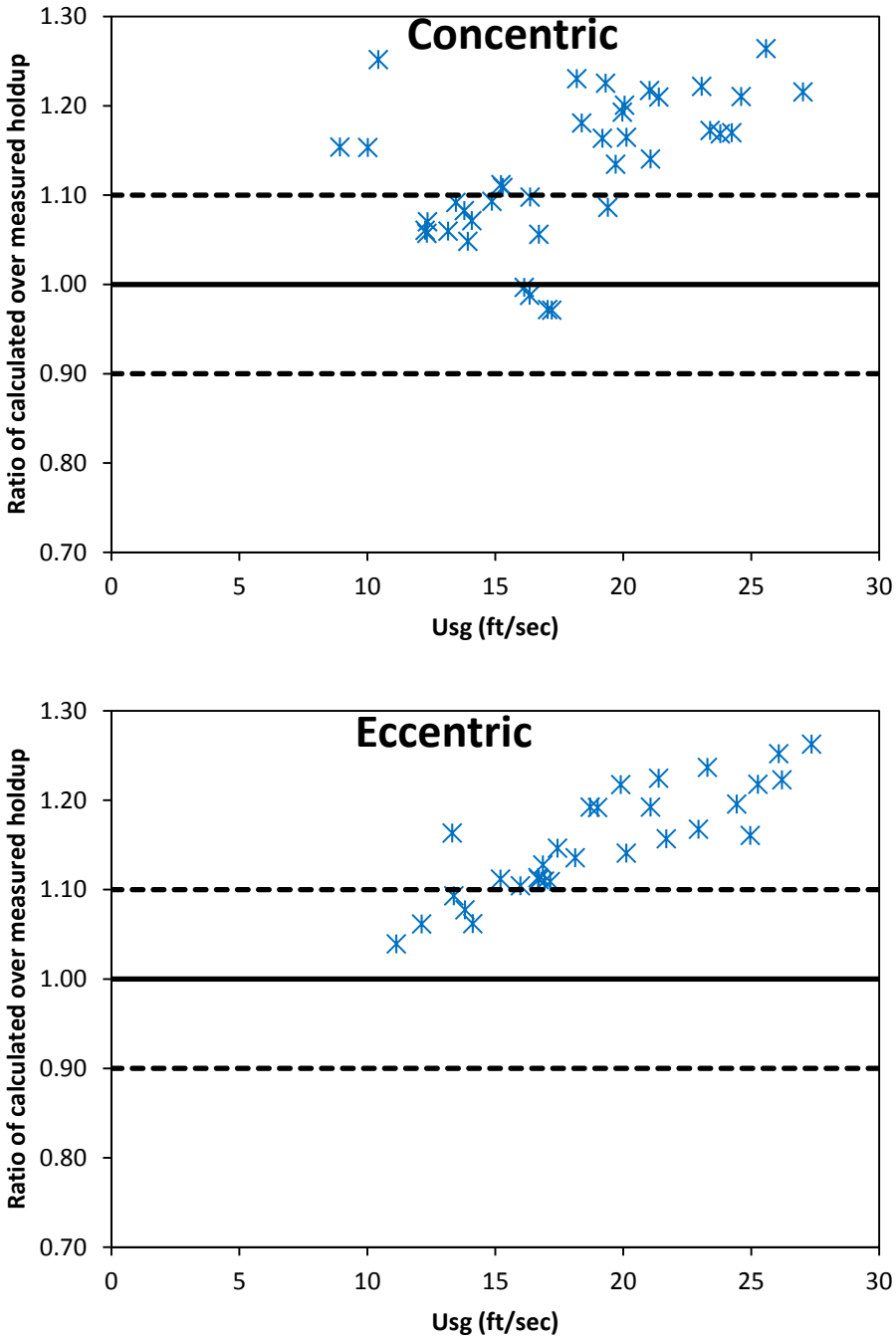


**Figure 33:** Holdup ratios between those estimated by mechanical analysis and the ones measured with TowerLab. The bulk line represents the equality between values and the dashed lines represent a 10% error margin from the equality line.

The results shown in Figure 33 reveal that only 36.4 and 14.7 % of the holdups calculated from mechanical analysis lay between the ±10%-interval from the value measured for the concentric and eccentric cases. However, when we analyze only the ratios for gas superficial velocities below 20 ft/sec, these values increase to 59.3 and 27.8%, respectively. The reason of this lack of accuracy can be explained by two factors: first, the uncertainty of holdup measurements, and second, the overestimation of the friction losses. If we apply the same principle as before, but ignore all losses due to friction, we obtain the graphs shown in Figure 34. In this plot, the accuracy in the concentric case grows to 72.7%, whereas in the eccentric scenario we reach 79.4%. Even though friction is important in this study, it is the only variable that is measured by the tests and thus where the highest uncertainties lay.

**Computer simulations using OLGA 7**

A similar comparison to the one described on the paragraph above was made with the OLGA results. Not all tests could be compared because OLGA failed to simulate three of the concentric cases and one of the eccentric scenarios. In all cases, the mass air rate was below 250 kg/h, which caused instability in the program's routine. A surface tension related error was indicated by the software; however no further detail was given, or could it be found in the User Manual.

From the tests that could be compared, the results differ from the laboratory experiment significantly. There seems to be a correlation between the experiments and the results given by OLGA, which would require further exploring the software's capabilities, but that would be out of the scope of this work.

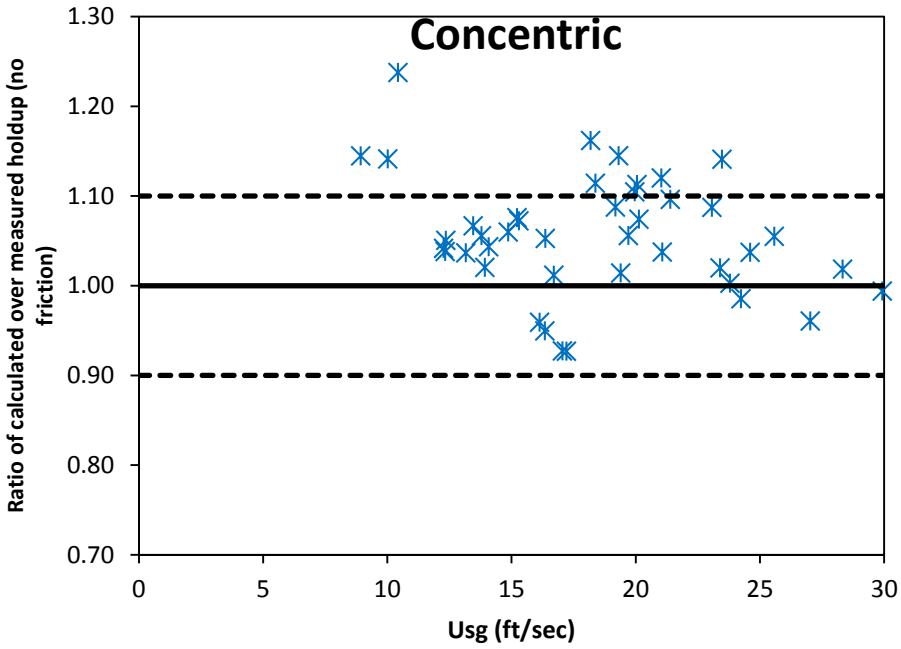


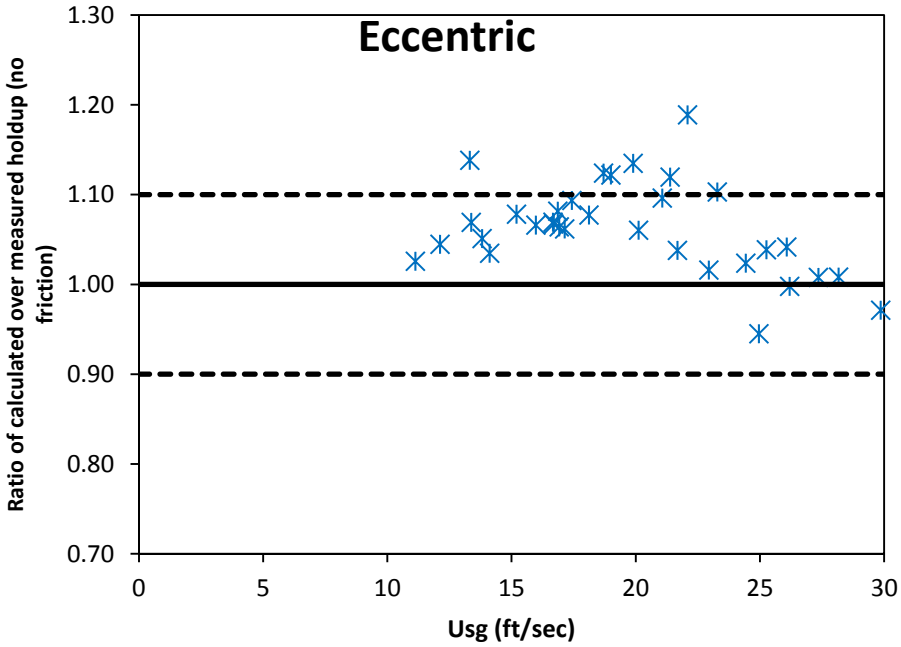


**Figure 34:** Holdup ratios between those estimated by mechanical analysis without friction and the ones measured with TowerLab. The bulk line represents the equality between values and the dashed lines represent a 10% error margin from the equality line.

Figure 35 shows the ratio of the average holdup values given by OLGA 7 and those measured on TowerLab. Only 14.6 % of the results are with the 10 % error margin in the concentric case (top of Figure 35), whereas in the eccentric case, this value corresponds to 24.2 % of the simulations. When this statistical study is limited to tests where the gas superficial velocities are below 20 ft/sec, an improvement is seen, but it is still not satisfactory: 25.0 and 41.1 % of the tests in the concentric and eccentric configurations, respectively.

Similarly, the pressure drop gradients are compared and the ratio between OLGA and measured values are plotted against gas superficial velocities in Figure 36. In this case, OLGA has consistently overestimated the pressure gradient, with nearly all ratios being above the +10%-line. However, the ratios seem to fall under a nearly horizontal trend, indicating that the results obtained by OLGA and those measured are correlated. With that observation in mind, we excluded the pressure losses given by OLGA and plotted the graph again, resulting in Figure 37. When excluding the friction losses, the accuracy of OLGA is visibly better: 29.3 and 39.4% of the results are within the ±10% lines for concentric and eccentric cases, respectively. When considering only those points below the 20 ft/sec threshold, the accuracy is improved to 50.0 and 76.5%, respectively.

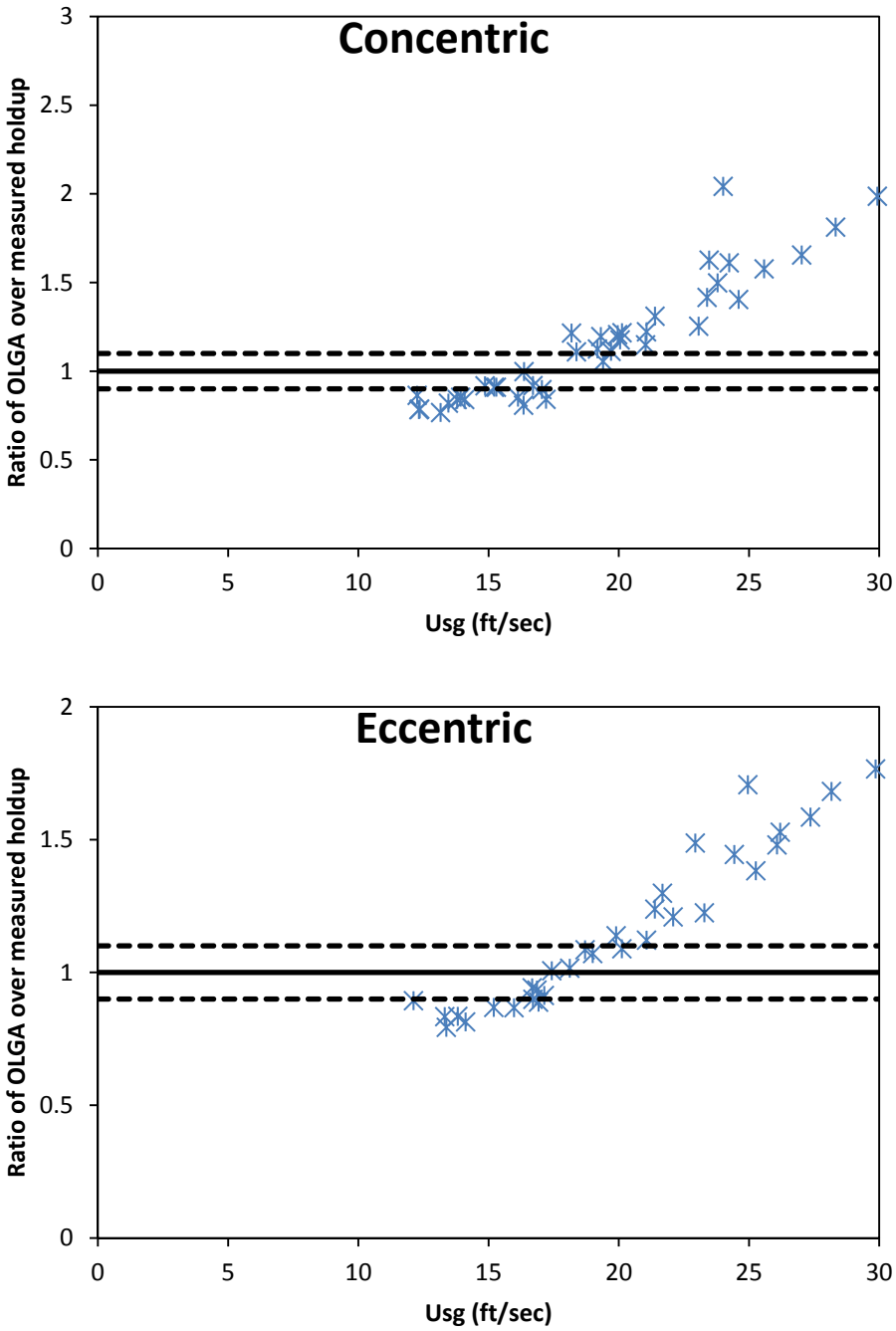


**Figure 35:** Holdup ratios between those calculated by OLGA 7 and the ones measured with TowerLab. The bulk line represents the equality between values and the dashed lines represent a 10% error margin from the equality line.

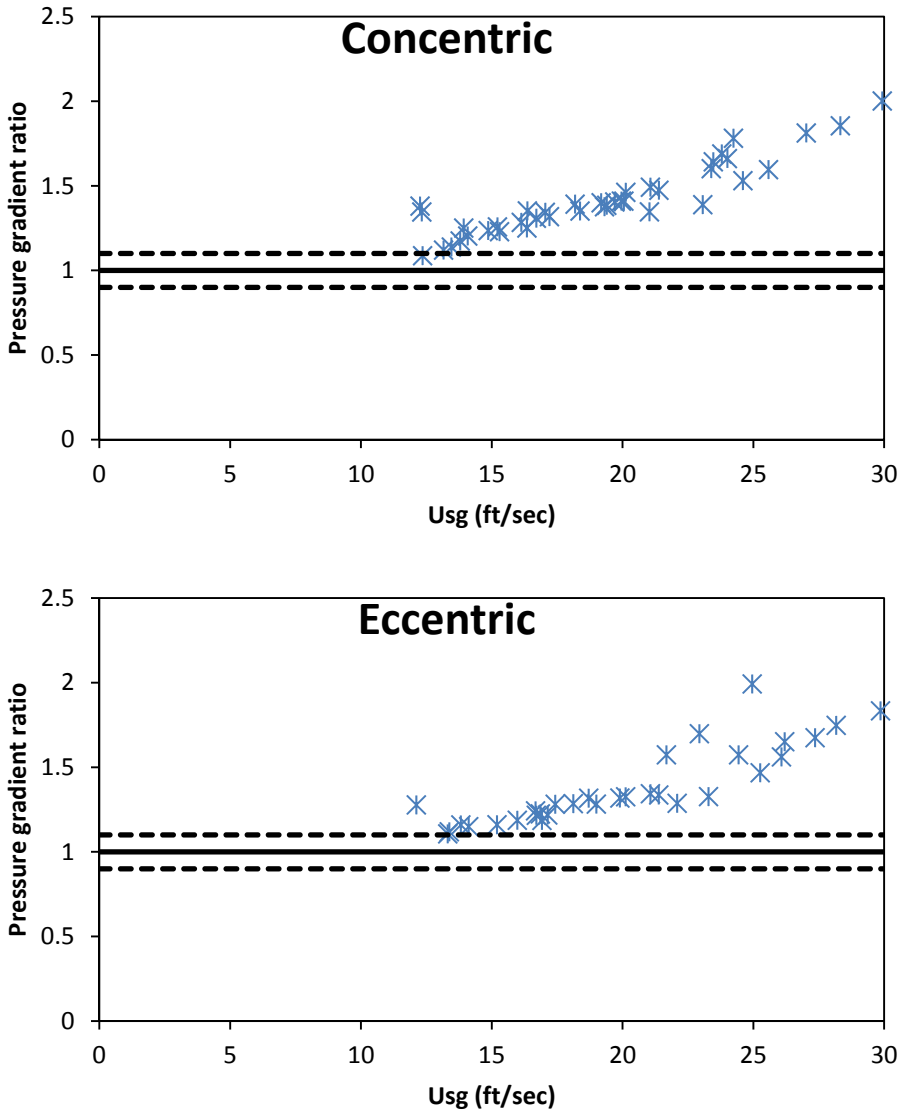


**Figure 36:** Pressure gradient ratios between those calculated by OLGA 7 and the ones measured with TowerLab. The bulk line represents the equality between values and the dashed lines represent a 10% error margin from the equality line.

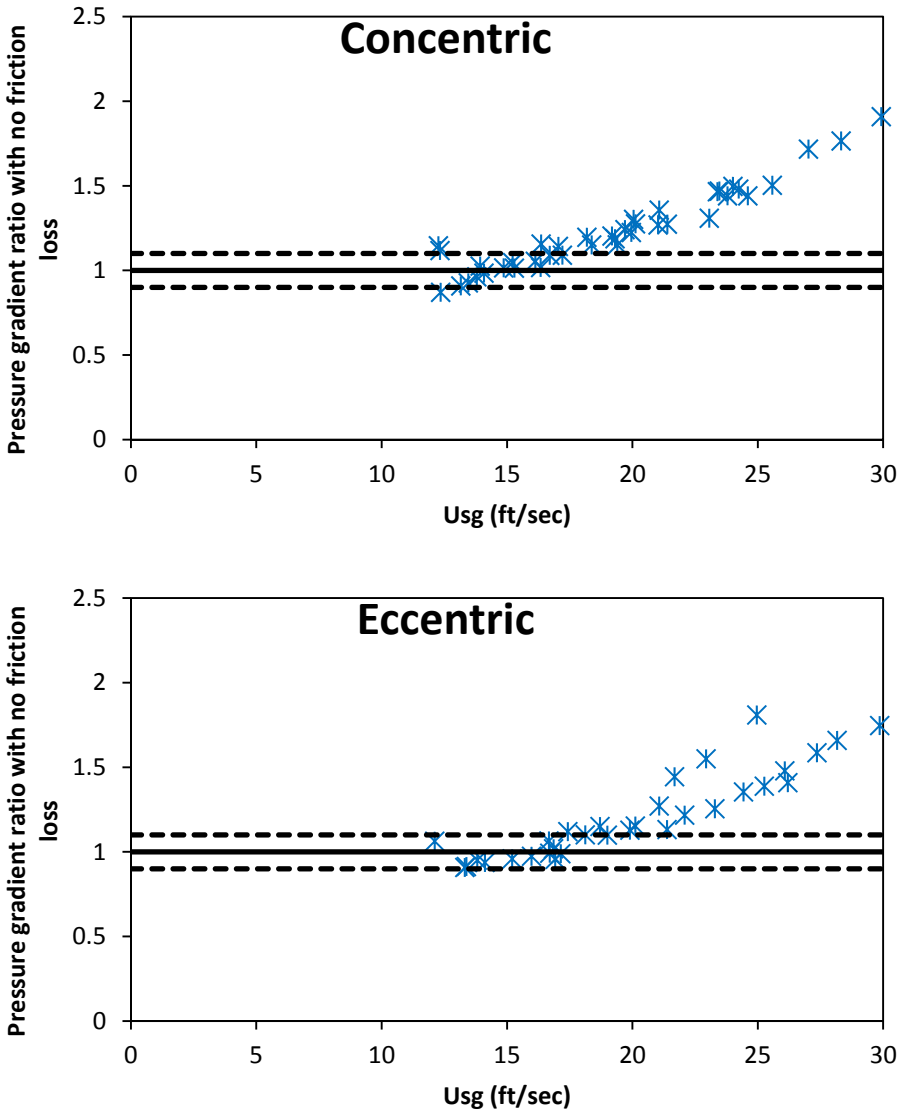


**Figure 37:** Pressure gradient ratios between those calculated by OLGA 7 without friction losses and the ones measured with TowerLab. The bulk line represents the equality between values and the dashed lines represent a 10% error margin from the equality line.

# CHAPTER VI

# CONCLUSIONS

This study investigated the two-phase flow inside the annular space. Three different scenarios were tested: steady-state in concentric and eccentric annulus, cyclic change in the air/water ratio for hysteresis analysis, and ramp-ups. From those experiments, we have learned:

- Reynolds, Weber and Froude numbers similar to the ones seen in the field can be reached with TowerLab, but not simultaneously. The facility geometry and its limitations, the ranges of pressure and temperature, and the fluids used are the reason why these two dimensionless parameters cannot be reproduced at the same time.
- Pressure drops in concentric and eccentric cases are statistically the same for the tested facility; however, a trend suggests the eccentric configuration causes higher pressure drops for gas superficial velocities less than 20 ft/s.
- Most of flow patterns seen are in the churn/slug region, with the transition zone between churn and slug being narrower in eccentric position. Annular flow cannot be reached with facility's present capability.
- The presence of couplings affects the stability of the Taylor bubble in seemingly slug flows.
- Local liquid accumulations are seen in the eccentric configuration around the coupling on the tubing.

- In hysteresis tests, pressure drop always reached the initial steady state values if time was allowed. That indicates that, when varying the liquid rate, time to reach steady state is only dependent on the constant air rate and the length of the casing.
- Ramp-up slope does not affect the final steady-state.
- Pressure drop spikes at the start of ramp-up mainly depend on the ramp slope value. The pressure spikes do not seem to be related to the surge of air into the system.

**Applicability to field situations**

The importance of these conclusions in the real life situations are as follows:

- In ramp-up scenarios, faster valve openings represent earlier steady-states, but they may also create uncontrolled flow of liquid toward the top of the casing. Given the observations taken from TowerLab, we can speculate that, for long casing lengths, the influx of high volumes of fluids may push the liquid phase up, towards the top, but it may not have enough energy to eject the liquids out of casing. Once the liquid phase reaches the top, local liquid accumulation may be seen around the couplings, causing unexpected pressure drops.
- In ramp-up scenarios, lower slopes will lead to smoother transitions. Nevertheless, the system requires more time to reach steady-state.
- At larger scale, tubing eccentricity will likely cause higher pressure drops for low gas superficial velocities than concentric tubing configurations.

- The accumulation of liquid around couplings may be more significant as the scale gets larger. The accumulated liquid in the annulus may be associated with the reduction in production.

**Future work**

Some steps can be taken to approach TowerLab even more to the reality of the field:

- Increase the air delivery capacity of the facility to reach annular flow and a wider range of possible air/water flow combinations.
- Change the diameter of the tubing inside TowerLab's casing to study the effects of the hydraulic diameter, eccentricity, and liquid accumulation around couplings.

Furthermore, we suggest the following points as future upgrades to TowerLab:

- Install flowmeters in the return lines.
- Measure in-situ liquid holdup.
- Measure how local liquid loading affects the flow of air through the annulus in concentric and eccentric configurations by running two-phase, steady-state flows and, after a certain time, stopping the input of water. See how pressure drop decreases with time.
- Implement a routine on LabView that controls tests by targeted mass rates and not by valve openings. This requires some automation and more experience with the operations, but it would allow for better quality data and more precise control.

# REFERENCES


Beggs, D.H. and Brill, J.P. 1973. A Study of Two-Phase Flow in Inclined Pipes. Journal of Petroleum Technology **25** (5): 607-617.

Caetano, E.F., Shoham, O., and Brill, J.P. 1992. Upward Vertical Two-Phase Flow Through an Annulus - Part 1: Single-Phase Friction Factor, Taylor Bubble Rise Velocity, and Flow Pattern Prediction. Journal of Energy Resources Technology 114: 1-13.

Das, P.K., Das, G., Purohit, N.K., and Mitra, A.K. 2002. Liquid Holdup in Concentric Annuli During Cocurrent (sic) Gas-Liquid Upflow. *The Canadian Journal of Chemical Engineering* **80** (1): 153-157.

Deuel, C.L., Chin, Y.D., Harris, J., Germanese, V.J., and Seunsom, N. 2011. Field Validation and Learning of the Parque das Conchas (BC-10) Subsea Processing System and Flow Assurance Design. Paper presented at the Offshore Technology Conference. OTC-21611-MS.

Economides, M.J., Hill, A.D., Ehlig-Economides, C., and Zhu, D. 2012. *Petroleum Production Systems*: Pearson Education. Original edition.

Ellul, I.R., Saether, G., and Shippen, M.E. 2004. The Modeling of Multiphase Systems Under Steady-State And Transient Conditions - A Tutorial. Pipeline Simulation Interest Group PSIG-0403.

Goldstein, R.J. 1996. *Fluid Mechanics Measurements*. Philadelphia, PA: Taylor & Francis. Original edition.

Hagedorn, A.R. and Brown, K.E. 1965. Experimental Study of Pressure Gradients Occurring During Continuous Two-Phase Flow in Small-Diameter Vertical Conduits. *Journal of Petroleum Technology* **17** (4): 475-484.

Hannisdal, A., Westra, R., Akdim, M.R., Bymaster, A., Grave, E., and Teng, D.T. 2012. Compact Separation Technologies and Their Applicability for Subsea Field Development in Deep Water. Paper presented at the Offshore Technology Conference. OTC-23223-MS.

Haynes, W.M. 2012. *CRC Handbook of Chemistry and Physics*. Boca Raton, FL: CRC Press. Original edition. p. 6-7 and 6-8.

Hoffman, J., Yun, H., Modi, A., and Pearce, R. 2010. Parque das Conchas Pipeline, Flowline and Riser System Design, Installation and Challenges. Paper presented at the Offshore Technology Conference. OTC-20650-MS.

IAPWS. 2003. *Revised Release on the IAPS Formulation 1985 for the Viscosity of Ordinary Water Substance*. Vejle, Denmark: The International Association for the Properties of Water and Steam. p. 7-10

Kiatrabile, T. 2012. Preliminary Study on Flow in Vertical Concentric Gas Annulus. MS Thesis, Texas A&M University, College Station, TX

Lage, A.C.V.M. and Time, R.W. 2000. An Experimental and Theoretical Investigation of Upward Two-Phase Flow in Annuli. Paper presented at the SPE Asia Pacific Oil and Gas Conference and Exhibition. SPE 00064525.

Lemmon, E.W. and Jacobsen, R.T. 2004. Viscosity and Thermal Conductivity Equations for Nitrogen, Oxygen, Argon, and Air. *International Journal of Thermophysics* **25** (1): 21-69.

Montgomery, D.C. and Runger, G.C. 2007. *Applied statistics and probability for engineers*: Wiley. Original edition.

NATO. 1994. *Quality assessment for wind tunnel testing*. Neuilly sur Seine, France. NATO, Advisory Group for Aerospace Research and Development. p. 19

Picard, A., Davis, R.S., Gläser, M., and Fujii, K. 2008. Revised Formula for the Density of Moist Air. *Metrologia* **45** (2): 149-155.

Schmelzer, J.W., Zanotto, E.D., and Fokin, V.M. 2005. Pressure Dependence of Viscosity. *J Chem Phys* **122** (7): 074511.

Shoham, O. 2006. *Mechanistic Modelling of Gas-Liquid Two-Phase Flow in Pipes*: Society of Petroleum Engineers. Original edition.

Szucs, A. and Lim, F. 2005. Heavy-Oil Gas Lift Using the Concentric Offset Riser (COR). Paper presented at the SPE/PS-CIM/CHOA International Thermal Operations and Heavy Oil Symposium. SPE/PS-CIM/CHOA International Thermal Operations and Heavy Oil Symposium SPE-97749-MS.

Taitel, Y., Bornea, D., and Dukler, A.E. 1980. Modelling Flow Pattern Transitions for Steady Upward Gas-Liquid Flow in Vertical Tubes. *Aiche Journal* **26** (3): 345-354.

Tavoularis, S. 2005. *Measurement in Fluid Mechanics*: Cambridge University Press. Original edition.

Waltrich, P.J., Falcone, G., and Barbosa Jr, J.R. 2013. Axial development of annular, churn and slug flows in a long vertical tube. *International Journal of Multiphase Flow* **57** (0): 38-48.

# APPENDIX

**Table A - 1:** Data from concentric tests.

| $\dot{m}_a$ (kg/h) | $\dot{m}_w$ (kg/h) | $u_{sg}$ (ft/s) | $u_{sl}$ (ft/s) | Holdup | Reynolds | Weber | Froude | $\Delta p_{39}$ (psi) | $\Delta p_{39}^{(\varepsilon)}$ (psi) |
|---|---|---|---|---|---|---|---|---|---|
| 191.4 | 530.6 | 8.9 | 0.060 | 0.18 | 7.13E+05 | 5.53E+03 | 14.2 | 8.2 | 8.5 |
| 212.9 | 213.1 | 10.4 | 0.024 | 0.16 | 8.00E+05 | 7.56E+03 | 19.2 | 7.9 | 8.2 |
| 213.3 | 519.4 | 10.0 | 0.058 | 0.18 | 7.91E+05 | 6.97E+03 | 17.8 | 7.9 | 8.2 |
| 254.1 | 397.7 | 12.3 | 0.045 | 0.17 | 9.46E+05 | 1.04E+04 | 26.6 | 6.8 | 7.1 |
| 265.5 | 583.6 | 12.3 | 0.065 | 0.16 | 9.51E+05 | 1.05E+04 | 27.0 | 6.8 | 7.0 |
| 273.9 | 754.1 | 12.4 | 0.085 | 0.16 | 9.48E+05 | 1.06E+04 | 27.2 | 6.7 | 7.0 |
| 293.7 | 753.2 | 13.2 | 0.084 | 0.16 | 1.00E+06 | 1.20E+04 | 30.8 | 6.4 | 6.7 |
| 297.4 | 715.5 | 13.5 | 0.080 | 0.15 | 1.00E+06 | 1.25E+04 | 32.2 | 6.3 | 6.6 |
| 305.9 | 732.9 | 13.9 | 0.082 | 0.14 | 1.02E+06 | 1.34E+04 | 34.5 | 5.8 | 6.1 |
| 306.2 | 613.2 | 14.1 | 0.069 | 0.15 | 1.04E+06 | 1.37E+04 | 35.2 | 6.0 | 6.3 |
| 307.7 | 746.5 | 13.8 | 0.084 | 0.15 | 1.02E+06 | 1.32E+04 | 33.8 | 6.1 | 6.4 |
| 320.9 | 580.5 | 14.9 | 0.065 | 0.14 | 1.07E+06 | 1.53E+04 | 39.2 | 5.8 | 6.0 |
| 324.0 | 248.8 | 16.3 | 0.028 | 0.14 | 1.20E+06 | 1.85E+04 | 47.1 | 5.4 | 5.7 |
| 328.0 | 556.9 | 15.3 | 0.062 | 0.13 | 1.09E+06 | 1.62E+04 | 41.5 | 5.7 | 5.9 |
| 334.2 | 394.2 | 16.1 | 0.044 | 0.14 | 1.18E+06 | 1.81E+04 | 46.0 | 5.4 | 5.7 |
| 334.5 | 640.7 | 15.2 | 0.072 | 0.13 | 1.08E+06 | 1.60E+04 | 41.1 | 5.7 | 6.0 |
| 353.2 | 500.8 | 16.7 | 0.056 | 0.13 | 1.17E+06 | 1.94E+04 | 49.4 | 5.2 | 5.5 |
| 358.9 | 374.3 | 17.2 | 0.042 | 0.14 | 1.24E+06 | 2.05E+04 | 52.3 | 5.1 | 5.3 |
| 388.0 | 926.0 | 16.4 | 0.104 | 0.12 | 1.12E+06 | 1.85E+04 | 47.6 | 5.1 | 5.4 |
| 390.5 | 273.8 | 19.4 | 0.031 | 0.11 | 1.23E+06 | 2.61E+04 | 66.3 | 4.3 | 4.6 |
| 394.6 | 701.1 | 17.0 | 0.079 | 0.13 | 1.21E+06 | 2.01E+04 | 51.5 | 5.0 | 5.2 |
| 409.8 | 586.9 | 18.4 | 0.066 | 0.11 | 1.16E+06 | 2.34E+04 | 59.8 | 4.7 | 4.9 |
| 423.5 | 100.6 | 24.2 | 0.011 | 0.07 | 1.12E+06 | 4.07E+04 | 103.3 | 2.6 | 2.9 |
| 430.6 | 715.8 | 18.2 | 0.080 | 0.10 | 1.11E+06 | 2.29E+04 | 58.6 | 4.6 | 4.9 |
| 435.5 | 581.5 | 19.2 | 0.065 | 0.10 | 1.17E+06 | 2.55E+04 | 65.1 | 4.3 | 4.6 |
| 449.1 | 607.4 | 19.3 | 0.068 | 0.10 | 1.15E+06 | 2.59E+04 | 66.0 | 4.4 | 4.6 |
| 454.1 | 570.7 | 20.0 | 0.064 | 0.09 | 1.17E+06 | 2.76E+04 | 70.5 | 4.1 | 4.4 |
| 459.2 | 419.1 | 21.4 | 0.047 | 0.08 | 1.17E+06 | 3.17E+04 | 80.8 | 3.6 | 3.9 |
| 465.1 | 209.6 | 23.8 | 0.024 | 0.07 | 1.16E+06 | 3.94E+04 | 99.7 | 2.8 | 3.1 |
| 466.1 | 590.0 | 20.1 | 0.066 | 0.09 | 1.17E+06 | 2.80E+04 | 71.6 | 4.0 | 4.2 |
| 470.8 | 791.0 | 19.7 | 0.089 | 0.10 | 1.22E+06 | 2.69E+04 | 68.8 | 4.3 | 4.5 |
| 524.8 | 419.7 | 23.5 | 0.047 | 0.06 | 1.07E+06 | 3.81E+04 | 97.2 | 2.9 | 3.2 |
| 544.1 | 413.4 | 24.0 | 0.046 | 0.05 | 9.32E+05 | 3.99E+04 | 101.7 | 2.8 | 3.1 |
| 552.1 | 760.8 | 21.1 | 0.085 | 0.09 | 1.21E+06 | 3.08E+04 | 78.6 | 3.7 | 4.0 |
| 555.8 | 1099.2 | 20.1 | 0.123 | 0.09 | 1.19E+06 | 2.79E+04 | 71.5 | 4.2 | 4.5 |

**Table A - 1:** Continued.

| $\dot{m}_a$ (kg/h) | $\dot{m}_w$ (kg/h) | $u_{sg}$ (ft/s) | $u_{sl}$ (ft/s) | Holdup | Reynolds | Weber | Froude | $\Delta p_{39}$ (psi) | $\Delta p_{39}^{(\varepsilon)}$ (psi) |
|---|---|---|---|---|---|---|---|---|---|
| 558.1 | 580.1 | 23.4 | 0.065 | 0.07 | 1.19E+06 | 3.79E+04 | 96.7 | 3.0 | 3.3 |
| 590.4 | 1133.1 | 21.0 | 0.127 | 0.09 | 1.25E+06 | 3.06E+04 | 78.6 | 4.2 | 4.5 |
| 596.8 | 784.6 | 23.1 | 0.088 | 0.08 | 1.25E+06 | 3.68E+04 | 94.2 | 3.6 | 3.9 |
| 601.4 | 601.2 | 24.6 | 0.067 | 0.07 | 1.23E+06 | 4.19E+04 | 106.9 | 3.0 | 3.3 |
| 605.3 | 514.9 | 25.6 | 0.058 | 0.06 | 1.18E+06 | 4.53E+04 | 115.5 | 2.8 | 3.0 |
| 607.4 | 188.9 | 29.9 | 0.021 | 0.04 | 1.03E+06 | 6.20E+04 | 157.6 | 1.8 | 2.1 |
| 610.5 | 296.2 | 28.3 | 0.033 | 0.05 | 1.09E+06 | 5.56E+04 | 141.3 | 2.1 | 2.4 |
| 611.0 | 404.3 | 27.0 | 0.045 | 0.06 | 1.17E+06 | 5.06E+04 | 128.7 | 2.3 | 2.6 |
| 617.5 | 99.3 | 32.5 | 0.011 | 0.03 | 8.35E+05 | 7.31E+04 | 185.5 | 1.5 | 1.8 |

**Table A - 2:** Data from eccentric tests.

| $\dot{m}_a$ (kg/h) | $\dot{m}_w$ (kg/h) | $u_{sg}$ (ft/s) | $u_{sl}$ (ft/s) | Holdup | Reynolds | Weber | Froude | $\Delta p_{39}$ (psi) | $\Delta p_{39}^{(\varepsilon)}$ (psi) |
|---|---|---|---|---|---|---|---|---|---|
| 243.4 | 593.6 | 11.1 | 0.067 | 0.19 | 8.96E+05 | 8.58E+03 | 22.0 | 7.8 | 7.5 |
| 257.0 | 399.7 | 12.1 | 0.045 | 0.18 | 9.57E+05 | 1.02E+04 | 26.0 | 7.4 | 7.1 |
| 300.3 | 794.6 | 13.4 | 0.089 | 0.15 | 1.01E+06 | 1.24E+04 | 31.9 | 6.5 | 6.3 |
| 303.6 | 592.4 | 14.1 | 0.066 | 0.15 | 1.06E+06 | 1.38E+04 | 35.3 | 6.2 | 5.9 |
| 305.0 | 907.8 | 13.3 | 0.102 | 0.15 | 9.88E+05 | 1.23E+04 | 31.7 | 6.6 | 6.3 |
| 308.2 | 757.7 | 13.8 | 0.085 | 0.15 | 1.04E+06 | 1.32E+04 | 33.9 | 6.3 | 6.0 |
| 313.9 | 104.9 | 16.9 | 0.012 | 0.13 | 1.18E+06 | 1.98E+04 | 50.4 | 5.5 | 5.2 |
| 326.5 | 386.6 | 16.0 | 0.043 | 0.14 | 1.15E+06 | 1.77E+04 | 45.1 | 5.8 | 5.5 |
| 328.0 | 578.3 | 15.2 | 0.065 | 0.14 | 1.11E+06 | 1.60E+04 | 41.0 | 6.0 | 5.8 |
| 328.3 | 197.1 | 17.1 | 0.022 | 0.13 | 1.19E+06 | 2.03E+04 | 51.8 | 5.4 | 5.1 |
| 331.2 | 292.6 | 16.7 | 0.033 | 0.13 | 1.17E+06 | 1.93E+04 | 49.2 | 5.5 | 5.3 |
| 356.0 | 480.3 | 16.9 | 0.054 | 0.13 | 1.17E+06 | 1.97E+04 | 50.3 | 5.4 | 5.2 |
| 393.5 | 892.0 | 16.7 | 0.100 | 0.13 | 1.17E+06 | 1.93E+04 | 49.4 | 5.5 | 5.3 |
| 410.0 | 688.2 | 18.1 | 0.077 | 0.12 | 1.20E+06 | 2.27E+04 | 58.2 | 5.0 | 4.7 |
| 424.3 | 605.0 | 19.0 | 0.068 | 0.11 | 1.21E+06 | 2.51E+04 | 63.9 | 4.7 | 4.5 |
| 426.2 | 499.1 | 19.9 | 0.056 | 0.10 | 1.21E+06 | 2.76E+04 | 70.0 | 4.5 | 4.2 |
| 427.7 | 312.9 | 21.4 | 0.035 | 0.09 | 1.22E+06 | 3.17E+04 | 80.6 | 4.0 | 3.7 |
| 436.6 | 983.7 | 17.4 | 0.110 | 0.12 | 1.18E+06 | 2.11E+04 | 54.0 | 5.2 | 4.9 |
| 448.8 | 777.3 | 18.7 | 0.087 | 0.11 | 1.18E+06 | 2.43E+04 | 62.1 | 4.7 | 4.5 |
| 450.1 | 603.2 | 20.1 | 0.068 | 0.10 | 1.26E+06 | 2.81E+04 | 71.6 | 4.4 | 4.1 |
| 461.8 | 101.0 | 26.2 | 0.011 | 0.06 | 1.17E+06 | 4.76E+04 | 120.7 | 2.5 | 2.3 |
| 465.5 | 209.6 | 24.4 | 0.024 | 0.07 | 1.20E+06 | 4.14E+04 | 105.1 | 2.9 | 2.7 |
| 551.8 | 404.1 | 25.0 | 0.045 | 0.06 | 1.09E+06 | 4.31E+04 | 109.8 | 2.3 | 2.0 |
| 552.7 | 610.8 | 22.9 | 0.068 | 0.07 | 1.14E+06 | 3.64E+04 | 93.0 | 2.9 | 2.6 |
| 554.3 | 776.7 | 21.7 | 0.087 | 0.08 | 1.17E+06 | 3.25E+04 | 83.2 | 3.4 | 3.1 |
| 595.1 | 1134.8 | 21.1 | 0.127 | 0.10 | 1.26E+06 | 3.07E+04 | 78.9 | 4.2 | 3.9 |
| 598.5 | 941.9 | 22.1 | 0.106 | 0.09 | 1.24E+06 | 3.38E+04 | 86.5 | 4.1 | 3.8 |
| 603.0 | 777.1 | 23.3 | 0.087 | 0.08 | 1.28E+06 | 3.75E+04 | 96.0 | 3.7 | 3.4 |
| 603.5 | 196.6 | 29.9 | 0.022 | 0.05 | 1.12E+06 | 6.17E+04 | 156.9 | 2.0 | 1.7 |
| 603.7 | 400.3 | 27.4 | 0.045 | 0.06 | 1.20E+06 | 5.21E+04 | 131.9 | 2.5 | 2.2 |
| 604.1 | 207.9 | 30.1 | 0.023 | 0.05 | 1.12E+06 | 6.28E+04 | 159.0 | 2.0 | 1.7 |
| 605.5 | 518.9 | 26.1 | 0.058 | 0.07 | 1.23E+06 | 4.73E+04 | 120.0 | 2.8 | 2.5 |
| 605.7 | 338.4 | 28.2 | 0.038 | 0.06 | 1.17E+06 | 5.52E+04 | 139.7 | 2.3 | 2.0 |
| 606.1 | 601.9 | 25.3 | 0.068 | 0.07 | 1.28E+06 | 4.44E+04 | 112.7 | 3.1 | 2.8 |